

https://dspace.org/

Characterisation of Standard Telecommunication Fibre Cables for Cost-Effective Free Space Optical Communication

Iga, Fortune Kayala

2024

University of the Witwatersrand, Johannesburg

https://hdl.handle.net/10539/45424

Iga, Fortune Kayala . (2024). Characterisation of Standard Telecommunication Fibre Cables for Cost-Effective Free Space Optical Communication [Masters dissertation, University of the Witwatersrand, Johannesburg]. https://hdl.handle.net/10539/45424

Downloaded from a DSpace repository. https://dspace.org/



UNIVERSITY OF THE
WITWATERSRAND,
JOHANNESBURG

Characterisation of Standard Telecommunication Fibre Cables for Cost-Effective Free Space Optical Communication

Fortune Kayala Iga

Supervisor: Dr. Mitchell A. Cox

A dissertation submitted to the Faculty of Engineering and the Built Environment, University of the Witwatersrand, Johannesburg, in fulfilment of the requirements for the degree of
Master of Science in Engineering.

2024

Declaration

I, the undersigned, hereby declare that the work contained in this thesis is my own original work and that I have not previously in its entirety or in part submitted it at any university for a degree.



Fortune Kayala Iga

Braamfontein, Johannesburg
October 4, 2024

Abstract

In an era marked by an escalating demand for high-speed internet connectivity, optical communication plays a crucial role in meeting these needs. Free Space Optical (FSO) communication, which involves the wireless transmission of optical signals through the atmosphere, holds promise for extending existing fibre optic networks and connecting individuals beyond current coverage areas. Despite the potential, commercial FSO systems remain prohibitively expensive.

A cost-effective FSO system can be achieved by utilising small form-factor pluggable (SFP) transceiver modules. These budget-friendly devices offer powerful transmit lasers and highly sensitive receiving photodiodes. To utilise these devices, optical signals are collimated out of a transmitting fibre into the atmosphere and coupled back into a receiving fibre. However, further investigation is needed to determine the optimal fibre cables for transmitting and receiving optical signals across the atmosphere to maximise received optical power and achieve efficient FSO communication.

This study aims to characterise the light coupling performance of standard telecommunication fibre cables, with a focus on the optical power transmitted from and received by the fibre cable under atmospheric conditions. The methodology employed for characterising the power transmitted by the fibre cables involves measuring the optical power in the fundamental Gaussian mode. This mode optimises transmission through the atmosphere by minimising beam divergence. Subsequently, light coupling from free-space is characterised by measuring the optical power coupled into the different fibre cables under non-ideal conditions, including misalignment and atmospheric turbulence.

The findings of this research show notable correlations between the physical attributes of the fibre cables, namely refractive index profile, core size and numerical aperture, and their transmission and reception performances. The comprehensive characterisations of the standard fibre cables presented in this study provide insights into their suitability for distinct roles within a low-cost FSO system.

Acknowledgements

I would like to express my sincere gratitude to the following individuals and organisations for their invaluable support and contributions to the completion of this dissertation:

First and foremost, I am deeply grateful to my supervisor, Dr. Mitchell Cox, for his unwavering guidance, patience, encouragement, and expertise throughout this research endeavour. His mentorship has been instrumental in shaping the direction of my research and fostering my personal growth as an engineer.

I am thankful to the African Laser Center for their generous financial support, which enabled me to pursue this research project and further my academic goals. Furthermore, I am indebted to the staff at the School of Electrical and Information Engineering whose assistance has been indispensable for the completion of this dissertation.

Special thanks to my collaborators, colleagues, and friends, Ultan, Alice, Steve, Mikaeel, and Kit, for their invaluable insight, constructive feedback and support during this research.

I am deeply grateful to my parents, Ngonya and Keletso Mokoena, and my siblings, Nalu and Karabo, for their unwavering support and understanding throughout this challenging journey. Their love and encouragement have been my source of strength and motivation. Without them, I would not have been able to navigate the highs and lows of the research process.

Finally, I would like to express my appreciation to all those who have played a role in the realisation of this dissertation. Your support, whether big or small, has been truly invaluable.

Contents

Declaration i

Abstract ii

Acknowledgements iii

List of Figures vi

List of Acronyms x

Resulting Publications xi
Journal Papers xi

1 Introduction 1
1.1 SFP transceiver-based FSO systems 3
1.2 Problem statement and research question 5

2 Background 6
2.1 Introduction to fibre optic cables 6
2.2 Gaussian beam propagation 8
2.3 Choice of lenses in a fibre-based FSO systems 9
2.4 Effects of atmospheric turbulence on optical signals 12
2.4.1 Loss of spatial coherence 13
2.4.2 Beam wander and angle-of-arrival fluctuations 13
2.4.3 Intensity fluctuations 14
2.5 Summary 15

3 Transmitter characterisation 16
3.1 Transmitted optical power 17
3.2 Modal decomposition of fields emitted from fibre cables 19
3.2.1 Experimental setup to conduct modal decomposition 20
3.2.2 Results and discussion 21
3.3 Conclusion 23

4 Receiver characterisation 25
4.1 Fibre coupling under misalignment 25
4.1.1 Experimental setups to test fibre coupling under misalignment 26
4.1.2 Effect of misalignment on coupled power 30
4.2 Fibre coupling in atmospheric turbulence 32

4.2.1 Simulation of atmospheric turbulence using Zernike polynomials . . . 33
4.2.2 Experimental set-up and calibration of turbulence phase screens 34
4.2.3 Effect of simulated turbulence on coupled power . . . 36
4.3 Conclusion . . . 38

5 Integrated Analysis of Transmitter and Receiver Performance 40
5.1 Unidirectional transmission . . . 41
5.2 Bidirectional transmission . . . 43
5.3 Conclusion . . . 45

6 Summary 47
6.1 Recommendations for future work . . . 49

References 51

List of Figures

1.1 FSO communication established using SFP transceivers and fibre cables. This can be done using standard (a) or Bidirectional (b) SFP transceiver modules. The fibre cables are used to transmit and receive the optical signals. 4

2.1 Structure of an optical fibre cable (a). Illustration of the acceptance angle (θ_a) in a step-index fibre. θ_a represents the propagation angle within the fibre, and n denotes the external refractive index(b). 7
2.2 Propagation of light rays in step index (a) and graded index (b) fibre cables 8
2.3 Collimated beam diameter at the transmit lens resulting from different focal lengths and fibre core sizes. 10
2.4 The power through a circular aperture. Only 86.5% of a beam's total power passes through a lens with a radius equal to its beam waist. . . . 11
2.5 Resultant Beam size along propagation caused by different initial beam sizes at the transmitter. The beam diameter at the transmitter is represented on the Y-axis, while the diameter at the receiver is shown using the heatmap. 11
2.6 Focal spot diameter (a) and lens numerical aperture (b) resulting from different focusing lens f-numbers. Parameters of standard fibre cables are represented using the asterisks. The yellow asterisk represents the single-mode fibre, the green asterisk represents the OM2 to OM5 multi-mode fibres, and the red asterisk represents the OM1 fibre cable. 12

3.1 Intensity images of beams launched from fibres cables when connected to an Small Form-factor Pluggable (SFP) transceiver module. 17
3.2 Experimental setup to measure power transmitted from SFP transceivers through the standard fibre cables. The fibre cables are manipulated during testing to induce mode coupling and bending losses. 18
3.3 Measurements of optical power transmitted through fibre cables when connected to two types of SFP transceiver modules labelled SFP A and B. The optical power is normalized to the power in the single-mode. 18
3.4 Experimental setup to perform modal decomposition of fields launched by fibre cables, represented as Tx Fibre. Lenses L1 and L2 are used as a 4F telescope, which mirrors M1 and M2 are used to align the beam to the SLM. Lens L3 performs a Fourier transform on the beam and separates the diffraction orders (0^{th}, 1^{st} and 2^{nd}). The 1^{st} diffraction order is observed with an intensity camera. 20

3.5 Average modal content of beams from SFP A. The modal content was averaged across 5 measurements. All fibre cables exhibited high Gaussian content. 21
3.6 Average modal content of beams from SFP B. The modal content was averaged across 5 measurements. All fibre cables exhibited high Gaussian content. 22
3.7 Average Gaussian content measured from fields launched out of the fibre cables. The single-mode fibre, represented by SM, records the highest Gaussian content. 22
3.8 Product of average Gaussian content and normalized optical power relative to the power transmitted by the single-mode fibre cable. The OM5 fibre cable records the highest Gaussian power. 23

4.1 Cartesian axes on the tip of a fibre cable (a) and angular misalignment on an incoming beam (b). 26
4.2 Experimental setup to observe the effects of lateral and angular misalignment on the power coupled into the standard fibre cables. SMF represents a single mode fibre while Rx Fibre represents the different fibre cables tested. M1, M2, M3 and M4 represent mirrors used for alignment. Lenses L1 and L2 of focal lengths 50 mm and 300 mm respectively, form a 4f expansion telescope system. Lenses L3 and L4 each have a focal length of 200 mm. Lens L5, with a focal length of 30 mm, focuses the beam onto the fibre cables. 27
4.3 A Gaussian mode hologram and diffraction grating encoded on the Spatial Light Modulator (SLM) screen (a). The grating frequency is increased to change the angle of the first order beam in order to impose focal point lateral displacement (b). The hologram is shifted to laterally shift the first order beam and impose tilt misalignment (c). A Fourier lens is encoded onto the SLM to impose longitudinal misalignment (d). . 28
4.4 Application of lateral displacement on the fibre tip. This is achieved by manipulating the grating frequency encoded on the SLM, resulting in the angular change $\Delta\beta$. The lateral offset on the fibre tips is represented by Δd. 29
4.5 Application of angular misalignment on the fibre tip. This is achieved by laterally displacing the beam on the SLM screen by ΔL. The resulting angular offset at the fibre tip is given by $\Delta\theta$ 29
4.6 Application of longitudinal misalignment on the fibre cable. This is achieved by encoding a Fourier lens onto the SLM, which is then relayed onto the receiving lens L5. The encoded lens and lens L5 emulate a compound lens with a variable focal length. 29
4.7 The impact of focal point lateral misalignment on coupling into standard fibre cables. The lateral shift ranges from -60 μm to 60 μm. Notably, the OM1 fibre cable demonstrates the highest average normalized power, whereas the single-mode fibre exhibits the least coupling under this misalignment condition. 31

4.8 The impact of focal point angular misalignment on coupling into standard fibre cables. As the angular offset increases, a decrease in coupled power is observed across all fibre cables. Among them, the OM1 fibre cable exhibits the highest average normalized power, while the single-mode fibre demonstrates the lowest under this misalignment. 31
4.9 Impact of longitudinal misalignment on coupling into standard fibre cables. The longitudinal offset varies within the range of -1.5mm to 1.5mm. Among the fibres, the OM1 fibre cable exhibited the highest average normalized power, while the single-mode fibre showcased the lowest. 32
4.10 Examples of generated Zernike polynomials which represent the following aberrations: piston (a), vertical tilt (b), horizontal tilt (c), oblique astigmatism (d), defocus (e) and vertical astigmatism (f). 33
4.11 Turbulent phase screens generated at different turbulence strengths. The phase spans from 0 to 2π. 34
4.12 Experimental setup to observe the effects of simulated turbulence on the power coupled into the standard fibre cables. SMF represents a single mode fibre while Rx Fibre represents the different fibre cables tested. M1, M2, M3 and M4 represent mirrors used for alignment. Lenses L1 and L2, each with a focal length of 150 mm, relay the beam from the collimator to the SLM. Lenses L3 and L4 each have a focal length of 200 mm. Lens L5, with a focal length of 30 mm, focuses the beam onto the fibre cables.The intensity camera replaces the receiving fibre (Rx Fibre) and the power meter during the calibration of turbulence strength. 35
4.13 Verification plot of the measured Strehl ratio (Strehl Ratio (SR)) against theoretical Strehl ratio. 200 measurements were made for each value of D/r_0. The errorbar represent standard error. 35
4.14 Effect of simulated turbulence on fibre coupling. The average power coupled at specific turbulence strengths is calculated across 100 measurements. The shaded region represents the standard error (a). Additionally, an average of the power coupled into each fibre cable across all turbulence strengths is presented (b). The OM1 fibre cable records the highest coupled power in the presence of simulated turbulence. 37
4.15 Verification plot of the measured Strehl ratio (SR) against theoretical Strehl ratio. The blue dots indicate the measured Strehl ratio in the absence of tilt aberrations. Excluding tilt results in weaker turbulence strength. 37
4.16 The effect of higher-order aberrations on fibre coupling. The phase screens generated excluded the low-order tilt aberrations. Average power coupled at specific turbulence strength is calculated across 100 measurements, with the shaded region representing the standard error (a). An average of the power coupled into each fibre cable across all turbulence strengths is presented (b). The OM1 fibre cable records the highest coupled power in the presence of higher-order modes. 38

5.1 Gaussian content in optical fields launched from the fibre cables (a). The product of the Gaussian content and the total power transmitted by the fibre cable relative the the total power transmitted by the single-mode fibre cable. 41
5.2 Average normalized power coupled into the fibre cables in the presence of simulated turbulence. The average power is calculated across all generated turbulence strengths. 41
5.3 Unidirectional transmission of a light beam from a transmit fibre to a receive fibre across a turbulent atmospheric channel. 42
5.4 Average received Gaussian power in the presence of atmospheric turbulence. This is calculated by multiplying the Gaussian content transmitted by the fibre cables, by the average power coupled into the fibre cables under simulated turbulence. The arrow points to the highest received power. 42
5.5 Average received Gaussian power in the presence of atmospheric turbulence, relative to the total power transmitted by the single-mode fibre. This is calculated by multiplying the Gaussian power relative to the total power transmitted by the single-mode power, by the average power coupled into the fibre cables under simulated turbulence. The arrow points to the highest received power. 43
5.6 Bidirectional transmission of two optical signals with different wavelengths across a turbulent atmospheric channel. Each fibre cable serves as both a transmitter and receiver. 44
5.7 Received Gaussian power transmitted in a bidirectional arrangement, in the case of equal transmitted power (a) and power normalized to the power transmitted by the single-mode fibre. 44
5.8 Experimental bidirectional Free Space Optical (FSO) system. The system utilises a plano-convex lens with a diameter of 75 mm and focal length of 200 mm. 44
5.9 Average received power measured in a real-world bidirectional FSO system. Average received power across different times of the day (a). Average received power in each fibre cable across all time intervals measured. 45

List of Acronyms

AoA Angle-of-arrival

DPSK Differential Phase-Shift Keying

FSO Free Space Optical

FWHM Full Wave Half Maximum

GaAs Gallium arsenide

GBIC Gigabit Interface Converter

He-Ne Helium Neon

MSA Multi-Source Agreement

NA Numerical Aperture

OAM Orbital Angular Momentum

RF Radio Frequency

ROSA Receiver Optical Sub-Assembly

SLM Spatial Light Modulator

SM-TEC Thermally-Expanded Core Single mode fibre

SNR Signal to noise ratio

SFP Small Form-factor Pluggable

SR Strehl Ratio

STG Satellite-to-Ground

TOSA Transmitter Optical Sub-Assembly

VCSEL Vertical Cavity Surface Emitting Laser

WDM Wavelength Division Multiplexing

Resulting Publications

Journal Papers

1. M. Lavery, U. Daly, F.K. Iga, A. Boldin, A. Vallance and M.A. Cox. "Low-complexity turbulence resilience enabled by a multi-mode bi-directional transceiver," In *Optics Express*, vol. 32, no. 20, pp.34314-34330, Sep. 2024.

Conference Proceedings

1. F.K. Iga and M.A. Cox, "Threading a Laser Through the Eye of a Needle: Multimode Fibre Coupling in Turbulence," In *SAIP Conference proceedings 2022 (SAIP2022)*, Jul. 2022.
2. M.A. Cox, M. Dindar and F.K. Iga, "Low-cost Free-Space Optical Communications with Commodity Hardware," In *Frontiers in Optics + Laser Science 2023 (FiO, LS)* JTu4A.72., Oct 2023.

CHAPTER 1

Introduction

The internet has become a vital aspect of modern life, significantly impacting the quality of life, opportunities, and personal development globally. Its benefits, including enabling remote work, online shopping, and distance learning, have made internet access essential in contemporary society [1]. Despite a 4.7% increase in global internet usage from 2022 to 2023, bringing the online population to 67% of the world's total, approximately 2.6 billion people still lack access to the internet. This digital gap is particularly pronounced in the least developed countries, highlighting the stark disparity between wealthier and poorer nations. While high-income countries boast a 93% internet usage rate, only 27% of the population in low-income countries have internet access. Regionally, Africa has the lowest internet penetration, with only 37% of its population online, compared to Europe's 91% connectivity [2]. Efforts to bridge this digital divide are crucial, as those excluded from the internet miss out on its socioeconomic benefits and often face social marginalisation [1].

The wide deployment of fibre cables has been instrumental in achieving high internet usage in developed countries [3]. This infrastructure development stands in contrast to the challenges faced in Africa, where internet penetration remains lower. Africa has seen an increase in the number of submarine connections since 2001, with multiple cables such as the West Africa Submarine cable link (SAT3), the Eastern African Submarine System (EASSy) cable, and others being established [4]. Despite these advancements, there are still challenges in deploying terrestrial fibre infrastructure to reach the end-user. While historic copper infrastructure exists, optical fibre has emerged as the most reliable transmission medium for modern backbone networks [5]. Delivering services over fibre to the end-user minimises loss in quality and data speed. However, the cost and complexity of upgrading from historical copper infrastructure have been limiting factors in the deployment of fibre optical cables [6]. Such deployment depends on several factors, including administrative regulations, operator investment capacity, and geographic conditions [5].

Unsurprisingly, the deployment of fibre cable is more widespread in urban areas, while availability remains sparse in rural regions [4]. Consequently, the limited accessibility to internet infrastructure outside urban and suburban areas widens the gap in internet usage between urban and rural populations. Africa exhibits the most pronounced gap, with 57% of internet usage concentrated in urban areas compared to 23% in rural regions [2]. Disparities in education, infrastructure, and healthcare further exacerbate the divide between urban and rural areas. These disparities have contributed to the ongoing rapid urbanisation in Africa and Asia, with projections indicating that two-thirds of the world's population will reside in urban areas [7]. Unfortunately, this rapid urbanisation results in the growth of

informal settlements which are lack basic services and infrastructural development. Such underprivileged settlements often exist adjacent to regions with robust fibre infrastructure. Extending existing fibre networks to these marginalised communities would promote digital inclusion and enhance education and employment opportunities [4].

While the installation of fibre cables to extend existing fibre networks is complex, expensive and time-consuming, Free Space Optical (FSO) communication provides a simpler deployment alternative [8–10]. FSO communication refers to the wireless transmission of information through light signals propagating in the atmosphere [11]. This technology could provide last-mile broadband access to unconnected communities adjacent to fibre infrastructure.

FSO communication offers several advantages over other wireless communication schemes used for last-mile broadband access, such as Radio Frequency (RF). FSO communication systems operate within the unlicensed portions of the infrared spectrum, reducing the initial setup cost and development time. Additionally, such systems experience lesser beam divergence than RF signals, which leads to higher intensity at the receiver. Narrower beam divergence also increases the security of FSO systems, as an eavesdropper needs to be physically close to the beam to intercept the signal. Such interception which would lead to drastic power loss at the receiver which would be easily detected. Furthermore, the higher carrier frequencies used in FSO provide higher modulation bandwidth than microwave and radio wave frequencies [12].

Significant progress has been made in the development of FSO systems since their inception in the mid-20th century. Following the introduction of the working laser in July 1960, Bell Labs scientists achieved a milestone by transmitting signals over a distance of 40 km using a ruby laser [13]. Subsequently, in 1962, M.I.T. Lincoln Lab successfully transmitted a television signal across a distance exceeding 48 km using a Gallium arsenide (GaAs) based LED. The advancement continued with the development of the Helium Neon (He-Ne) laser, which played a crucial role in FSO progress. In November 1962, a Hughes' group conducted a 30 km laser communication experiment by modulating the intensity of a radio frequency signal on a He-Ne laser beam. This was followed by Electro-Optics Systems' achievement in May 1963, where they transmitted a voice modulated He-Ne laser beam across a distance of 190 km. Japan's Nippon Electric Company marked a significant milestone in 1970 by commissioning the first FSO system capable of handling commercial traffic. This fully duplex system utilised a 632.8 nm He-Ne laser to transmit data over a distance of 14 km. For a comprehensive overview of the strides made in FSO development between 1960 and 1970, refer to Ref. [14].

Modern FSO systems leverage various properties of light to achieve high data rates across different transmission ranges. These properties, including amplitude, phase, polarization, and wavelength, serve as the foundation for a range of modulation and multiplexing techniques. Experimental systems have demonstrated the effective utilization of these properties through methods such as Quadrature Amplitude Modulation, Homodyne Binary Phase Shift Keying, Polarization Multiplexing, and Wavelength Division Multiplexing [15–22]. These techniques play a crucial role in enhancing the efficiency and performance of FSO communication systems.

Building on the advancements in FSO technology, numerous companies are actively engaged in developing commercial FSO systems for wireless transmission solutions. These companies include Canon, fSONA, LightPointe Communications, MRV, Novasol, Omnitek, Plaintree Systems, and Wireless Excellence, among others [10, 23]. However, commercial FSO systems are often expensive and inaccessible to low-income communities. The high cost stems from the use of specialised hardware components, similar to those found in fibre Ethernet architecture, to meet stringent performance standards. These components include high-power lasers and sensitive avalanche photodiode-based receivers. Additionally, Ethernet-based systems frequently encounter performance issues under sub-optimal conditions such as misalignment and atmospheric turbulence, primarily because their link-layer is inherently incompatible with such challenges [24]. Even minor random bit errors

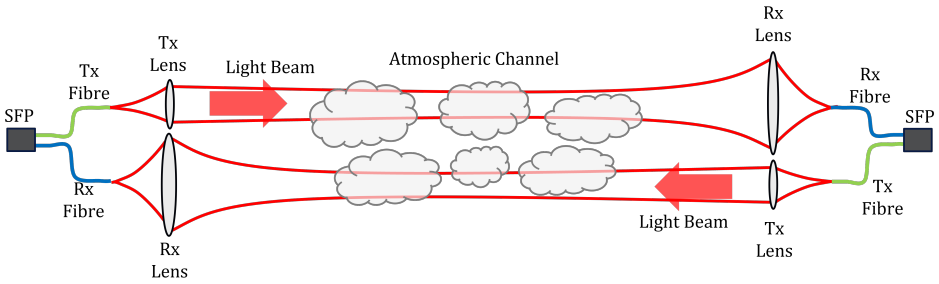
can trigger packet losses, significantly degrading service quality and potentially leading to connection disruptions. High-end FSO systems address these concerns with forward error correction algorithms and re-transmit schemes, contributing to their high cost. Moreover, FSO systems are not as widely adopted as other communication systems, resulting in lower production volumes and higher manufacturing costs per unit.

1.1 SFP transceiver-based FSO systems

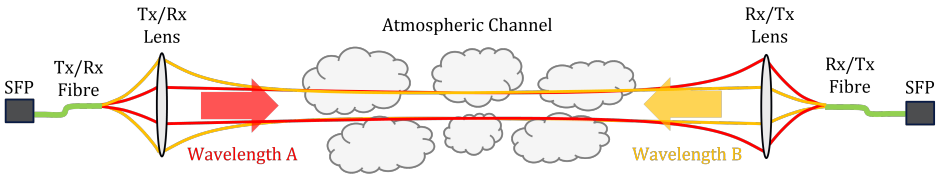
The integration of off-the-shelf telecommunication equipment in FSO systems can significantly lower their cost. Small Form-factor Pluggable (SFP) transceiver modules have received significant attention for this purpose. Commonly used in telecommunication networks, SFP transceivers are compact, hot-pluggable devices used to facilitate seamless conversions of Ethernet to optical signals in high-speed optical networks. They are designed to be smaller and cheaper than previous transceiver models such as the Gigabit Interface Converter (GBIC) [25, 26]. SFP transceivers support various data rates, making them suitable for enterprise networks and high performance data centres. Each transceiver consist of a Transmitter Optical Sub-Assembly (TOSA) and Receiver Optical Sub-Assembly (ROSA). The TOSA transmits a modulated beam produced by a Vertical Cavity Surface Emitting Laser (VCSEL), while a pin photodiode is used as a detector at the ROSA. Standard SFP modules have two separate ports for transmission and reception. Two fibre cables are used for upstream and downstream transmission, to connect the transmitter of one SFP module to the receiver of the other. However, the introduction of bidirectional SFP transceivers allows for one fibre cable to be used for both upstream and downstream transmission through Wavelength Division Multiplexing (WDM). Two distinct wavelengths are assigned for upstream and downstream transmission, resulting in a reduced number of fibre cables and overall costs in long transmission links [27]. Transceiver vendors have signed the Multi-Source Agreement (MSA), leading to standardised SFP transceiver sizes and the use of LC fibre connectors [28].

SFP transceivers can be used to establish an FSO link by propagating upstream and downstream optical signal through the atmosphere. In this set-up, a short piece of fibre cable channels light from the transmitter of an SFP into free space. The light beam is then collimated into the atmosphere with a lens and directed towards the second transceiver. At the receiver, a lens is used to collect and focus the light signal on the tip of a fibre cable which is connected to the receiver of the second SFP. The same is done for the downstream signal, as illustrated in Fig. 1.1(a), establishing the optical link. A similar FSO link can be established by leveraging bidirectional SFP modules. In this set-up, each transceiver would require one fibre cable to transmit and receive the dual wavelength light signals. One lens would be used at each transceiver to collimate transmitted signals while focusing received signals as illustrated in Fig. 1.1(b). While former system has the advantage of using the most suitable fibre cables for transmission and reception, the bidirectional system offers a cheaper option, as it uses half the number of fibre cables and lenses.

While fibre cables play a crucial role in such systems, coupling free-space light into an optical fibre cable is often difficult due to the strict alignment requirements. Previous studies extensively investigated the coupling efficiency of single-mode fibre cables due to their widespread compatibility with optic communication technology [29]. Despite their compatibility, single-mode fibres face difficulties in achieving high coupling efficiency, particularly in the presence of atmospheric turbulence, owing to their small core diameters and narrow numerical aperture. Ref. [30] highlighted a rapid degradation in the coupling efficiency of single-mode fibres under increased turbulence strength. This degradation was attributed to reduced spatial coherence caused by atmospheric turbulence. The effects of turbulence on fibre-coupled Differential Phase-Shift Keying (DPSK) for Satellite-to-Ground (STG) downlink were explored in Ref. [31], revealing how turbulence-induced phase distortion degrades spatial coherence and limits the coupling efficiency of single-mode fibre cables. Furthermore,



(a) Standard SFP-based FSO system



(b) Bidirectional SFP-based FSO system

Figure 1.1: FSO communication established using SFP transceivers and fibre cables. This can be done using standard (a) or Bidirectional (b) SFP transceiver modules. The fibre cables are used to transmit and receive the optical signals.

Toyoshima et al. [32] demonstrated the adverse impact of random angular jitter on coupling efficiency, emphasising the importance of optimising beam size during the coupling process.

In contrast to single-mode fibres, multi-mode fibre cables exhibit higher coupling efficiency due to their larger core diameters. Zheng et al. [29] compared the coupling efficiencies of single-mode fibre, 2-mode fibre, and 4-mode fibre at different turbulence strengths, highlighting the superior coupling efficiency of the 4-mode fibre. Additionally, Ref. [33] demonstrated the higher coupling efficiencies of few-mode fibre cables over signal-mode fibres, attributing this to their larger core sizes. Multi-mode fibre cables have also shown greater resilience to coupling light in the presence of atmospheric turbulence for quantum communication as seen in Ref. [34]. However, coupling light into a multi-mode fibre cable remains a delicate process, with power loss resulting from numerical aperture mismatch and alignment errors [35].

Different types of fibre cables have been employed in various SFP transceiver-based FSO systems. Single-mode fibre cables with SC connectors are used to guide light signals in and out of bidirectional SFP modules across a 125 m FSO link in Ref. [36]. However, using a single-mode fibre to capture light from free space limits the performance of such a FSO system. Multi-mode fibre cables offer improved light coupling due to their larger dimensions. This is demonstrated in the construction of a 1 Gbps FSO system developed in Ref. [37], where a 1 mm core size multi-mode fibre is used to couple optical signals from free-space into an SFP transceiver. A steerable short-range FSO system is developed in Ref. [38], which uses a 50 μm core multi-mode fibre to capture the optical signals and channel them to an SFP transceiver. This system achieves 10 Gbps transmission across 200 m of free-space. In another approach, a self-aligning FSO system is presented in [39], which implements spatial division multiplexing by using 8 multi-mode fibre cables with core sizes of 50 μm to capture and channel optical signals to 8 separate SFP transceivers.

While larger multi-mode fibre cables enhance fibre coupling at the receiving end, they may not be optimal for transmission at the sending end. Multi-mode fibres are susceptible to modal coupling and inter-modal dispersion, leading to distorted wavefronts and reduced beam quality [40, 41]. In contrast, single-mode fibre cables are specifically designed to exclusively transmit the fundamental Gaussian mode. Both types of fibre cables can be

leveraged in an FSO system, by transmitting from a single-mode fibre and receiving from a multi-mode fibre, as illustrated in Ref. [42].

1.2 Problem statement and research question

Fibre cables play a crucial role in transmitting and receiving optical signals in SFP-based FSO communication systems, as shown in Fig 1.1. However, with the wide variety of available fibre cables, ranging in specifications such as core size, numerical aperture, and graded-index profiles, it remains unclear which type(s) might be best suited for transmit and receive coupling. While previous studies have indicated the fibre cable parameters used in their systems, they seldom mention the specific fibre types [37–39]. Furthermore, to date there has been no comparative study carried out to determine which fibre cables that should be used in such systems. This gap in knowledge is critical, given that inefficient fibre coupling stands as the primary contributor to power loss in SFP-based FSO systems [37].

This study seeks to bridge this gap by comparing the performance of different fibre cables within this application context. The scope of this research is narrowed to standard telecommunication fibre cables defined in the international standard of Information Technology (Generic cabling for customer premises (ISO/IEC 11801)) [43]. These general-purpose telecommunication fibre cables include the single-mode and five classes of multi-mode fibre cables (OM1, OM2, OM3, OM4, and OM5). These form the core of typical short-range links in commercial data centre infrastructure [44]. These fibre cables are low-cost and readily available, making them advantageous for a cost-effective FSO system. Given the relatively low data rates involved in SFP-based FSO systems (in the order of gigabits per second) and the short fibre lengths at the transmitter and receiver, the effects of dispersion are neglected in this study.

The research question guiding this study is: ***"How do different telecommunication fibre cables compare in terms of transmit performance and free-space coupling performance?"***

To further refine this broad research question, the definition of "performance" used in this context is as follows: transmit performance refers to the ability of the fibre cables to transmit high optical power into free-space with minimal beam divergence. While free-space coupling performance refers to the ability of the fibre cables to couple as much light as possible from free-space, particularly under non-ideal conditions which are misalignment and atmospheric turbulence.

To fully explore the above stated research question, the following objectives are defined.

1. To determine the average optical power transmitted in the fundamental Gaussian mode (minimal divergence). This analysis relates to the transmit performance and is presented in Chapter 3.

2. To experimentally assess the effect of misalignment and atmospheric turbulence on the power coupled from free-space into the fibre cables. This analysis pertains to the free-space coupling performance and will be characterised in Chapter 4.

As discussed earlier, an opportunity arises when utilising an off-the-shelf bidirectional SFP transceiver, as it allows for the use of a common transmit/receive aperture. This approach significantly simplifies alignment and reduces costs, making it ideal for a low-cost system aimed at helping bridge the digital divide. Chapter 5 explores this approach further by jointly considering the transmit and free-space coupling performance characteristics.

CHAPTER 2

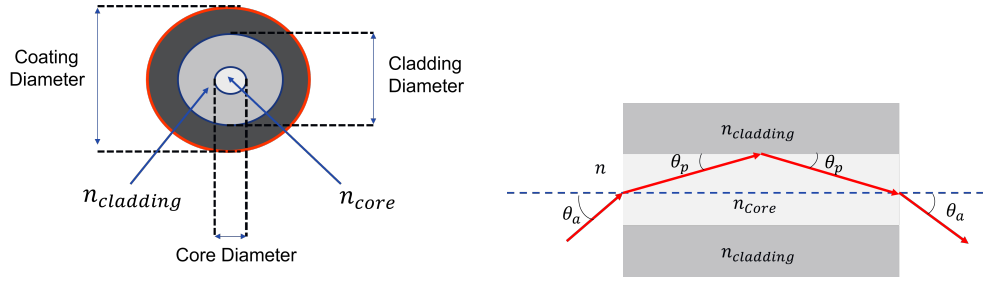
Background

Free Space Optical (FSO) systems offer high-speed data transmission across several kilometers by beaming light through the atmosphere. Like any communication system, FSO links consist of three basic parts: the transmitter, channel, and receiver. At the transmitter, a laser diode or high-intensity LED is typically used to generate the modulated light beams, which are expanded and collimated into the atmosphere using a series of lenses [12]. These light signals face many attenuating factors within the atmosphere which include natural divergence, scattering and absorption, and turbulence. The receiver often comprises lenses arranged in a telescope to capture as much light as possible, and focus it on a photo-diode for optical-to-electrical conversions [6]. There has been growing interest in the use of Small Form-factor Pluggable (SFP) transceiver modules for FSO applications [36, 37, 39, 42], which are readily available and low-cost.

The purpose of this background chapter is to highlight key design considerations in the development of a low-cost FSO system using SFP transceiver modules and fibre cables. The working principle and the variety of fibre cables are presented in Sec. 2.1. Sec. 2.2 presents the propagation of a Gaussian beam in free space, highlighting its natural divergence during propagation. The crucial role the optical lenses play in achieving efficient transmission is discussed in Sec. 2.3. Finally, the effects of atmospheric turbulence on propagating light signals are discussed in Sec. 2.4.

2.1 Introduction to fibre optic cables

Fibre Optic cables are cylindrical dielectric wave guides used to transport information in the form of optical energy. Fibre cables consist of three main concentric layers: the core, cladding, and coating, as depicted in Fig 2.1(a). The core, typically composed of low-loss silica glass and index-modifying dopants, is the central region through which light is guided. Surrounding the core is the cladding, which is made of a similar material but with a slightly lower refractive index. The outermost layer is the protective coating, which is a cushioning polymer that shields the silica structure from physical and environmental damage. Additional protection is often provided by an outer coating reinforced with steel or Kevlar material.



(a) Structure of an optical fibre cable (b) Total internal reflection

Figure 2.1: Structure of an optical fibre cable (a). Illustration of the acceptance angle (θ_a) in a step-index fibre. θ_a represents the propagation angle within the fibre, and n denotes the external refractive index(b).

Light in an optical cable travels through the fibre core, guided by the principle of total internal reflection. The acceptance angle, illustrated in Fig. 2.1(b), dictates the range of angles within which launched light must fall to be guided through the fibre. The Numerical Aperture (NA), a dimensionless parameter, characterizes this acceptance angle and is defined as

$$\text{NA} = \sqrt{n_{\text{core}}^2 - n_{\text{cladding}}^2} = \sin(\theta_a), \tag{2.1}$$

where θ_a is the acceptance angle, n_{core} is the refractive index of the core, and n_{cladding} is the refractive index of the cladding [45].

The guided paths of light within a fibre, known as modes, depend on the fibre type. Single-mode fibres support only one mode of light, with small core sizes (typically 8 μm to 10 μm) and numerical apertures around 0.1. In contrast, multi-mode fibre cables support multiple rays of light, featuring larger core sizes (e.g., 50 μm and 62.5 μm) and higher numerical aperture values, typically above 0.2.

The number of modes supported by a fibre is characterized by its normalized optical frequency or V-number, defined as

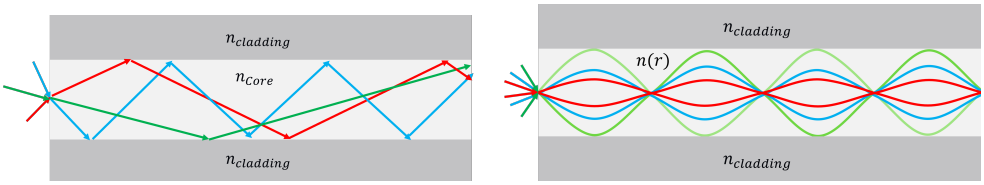
$$V = \frac{2\pi a}{\lambda}\text{NA}, \tag{2.2}$$

where a is the core size, λ is the wavelength of the light, and NA is the numerical aperture [46]. For single-mode fibres, the V-number is kept below 2.405. The estimated number of modes for multi-mode fibres is given by

$$M \approx \frac{g}{g+2} \cdot \frac{V^2}{2}, \tag{2.3}$$

where g is the refractive index profile exponent [45].

The movement of light within a fibre depends on its refractive index profile. There are two types of profiles: step-index and graded-index. In a step-index profile, the refractive index of the core is uniform across its entire radius, leading to modal dispersion—a distortion arising from varying propagation velocities of different modes within a multi-mode fibre. This is illustrated in Fig 2.2(a). To mitigate modal dispersion, graded-index profiles were introduced. These profiles gradually decrease the refractive index as the radial distance from the centre increases, allowing smoother transitions at the core-cladding boundary. Light rays in graded-index fibres propagate in a sinusoidal pattern, as shown in Fig 2.2(b) [40]. Graded-index fibres can transport larger amounts of data across longer distances with lower distortion compared to step-index fibres.



(a) Step index fibre (b) Graded index fibre

Figure 2.2: Propagation of light rays in step index (a) and graded index (b) fibre cables

The refractive index of graded-index fibre cores follows a power-law distribution given by

$$n(r) = \begin{cases} n_{\text{core}}\sqrt{1-2\Delta\left(\frac{r}{a}\right)^{g}}, & \text{for } r \leq a, \\ n_{\text{core}}\sqrt{1-2\Delta}, & \text{for } r > a, \end{cases} \tag{2.4}$$

where $\Delta = \frac{n_{\text{core}}^2 - n_{\text{cladding}}^2}{2n_{\text{core}}^2}$, a is the core radius, r is the radial distance from the centre, and g is the profile exponent. The graded-index profile can be adjusted by changing the profile exponent g [45].

Along with the standard single-mode fibre, there are five classes of graded-index multi-mode fibre cables (OM1 to OM5) which are standardised for use in telecommunication networks. The characteristics of the five multi-mode fibre cable classes are summarised in Table 2.1. The modal bandwidth has been improved by optimising the graded-index profiles, with the latest fibre type, the OM5 having the highest modal bandwidth. Being low-cost and readily available, these cables could be good candidates for use in a low-cost FSO systems.

Table 2.1: Characteristics of the 5 Multi-mode fibre cable Classes.

Class	Colour Code	Core Diameter	NA	Modal Bandwidth
OM1	Orange	62.5 μm	0.275	200 MHz*km
OM2	Orange	50 μm	0.2	500 MHz*km
OM3	Aqua	50 μm	0.2	2000 MHz*km
OM4	Aqua	50 μm	0.2	4700 MHz*km
OM5	Lime Green	50 μm	0.2	28000 MHz*km

2.2 Gaussian beam propagation

The fundamental Gaussian beam is the lowest order transverse electromagnetic wave and simplest beam type. It is often the desired output of laser sources as it focuses into the most concentrated focal spot [47]. At a wavelength of λ, the amplitude and phase profile of a Gaussian beam are described by the function [48]

$$U(x,y,z) = A_0 \frac{\omega_0}{\omega(z)} \exp\left[-\frac{x^2+y^2}{\omega^2(z)} - \mathrm{i}\left(kz + k\frac{x^2+y^2}{2R(z)} + \zeta(z)\right)\right]. \tag{2.5}$$

In this function, k is the wave number given by $\frac{2\pi}{\lambda}$, x and y are the transversal dimensions and z is the axial dimension. ω_0 represents the beam radius at the origin, where the beam is at its minimum size. This radius is also known as the beam waist. The physical bounds of a

Gaussian beam are theoretically infinite, however, the beam radius is commonly defined as the distance from the centre of the beam to the point where the amplitude is attenuated to $1/e^2$ of its maximum. The beam radius at different points of along the propagation direction is given by $\omega(z)$, which is

$$\omega(z) = \omega_0 \sqrt{1 + \left(\frac{z}{z_R}\right)^2}. \tag{2.6}$$

The Rayleigh range, represented by z_R, the distance along the propagation direction where the beam waist expands by a factor of the square root of two and is expressed as [8]

$$z_R = \frac{\pi \omega_0^2}{\lambda} \tag{2.7}$$

As the beam propagates, it tends towards a constant divergence angle given by

$$\Theta = \frac{\lambda}{\pi \omega_0}. \tag{2.8}$$

From this relationship, it should be noted that a larger beam waist would lead to less divergence during propagation than a smaller beam waist.

In Eq. 2.5, $R(z)$ represents the wavefront curvature radius, which is given by

$$R(z) = z \left[1 + \left(\frac{z_R}{z}\right)^2\right]. \tag{2.9}$$

The curvature radius is infinity at the origin, allowing for the plane wave approximation, which is valid for

$$\frac{\lambda z}{\pi \omega_0} \ll 1. \tag{2.10}$$

$\zeta(z)$ represents the phase retardation which is expressed as

$$\zeta(z) = \arctan\left(\frac{z}{z_R}\right). \tag{2.11}$$

The intensity of a Gaussian beam, which is the square of the amplitude ($I = |U|^2$), is derived from Eq. 2.5 to give

$$I(x, y, z) = |A_0|^2 \left[\frac{\omega_0}{\omega(z)}\right]^2 \exp\left[-\frac{2(x^2 + y^2)}{\omega^2(z)}\right]. \tag{2.12}$$

Here, $|A_0|^2$ is the on-axis intensity, while the beam radius is the distance from the centre to the point where the intensity attenuates to approximately 13.5% of the maximum intensity $1/e^2$. Another common measure of the beam size is the radius from the centre to the point where the intensity drops to 50% of its maximum. This is known as the Full Wave Half Maximum (FWHM).

2.3 Choice of lenses in a fibre-based FSO systems

In a fibre-based FSO system, lenses are used to collimate light signal launched from transmitting fibres into free space and to focus these signals from free space onto the tips of receiving fibre cables. The choice of lenses used in an FSO system is crucial for efficient performance, as they affect both transmitted and received power. There is a variety of standard lenses readily available on the market, which vary in diameter and focal length. Common diameters are 25.4 mm (1"), 50.8 mm (2"), and 75 mm, while typical focal lengths

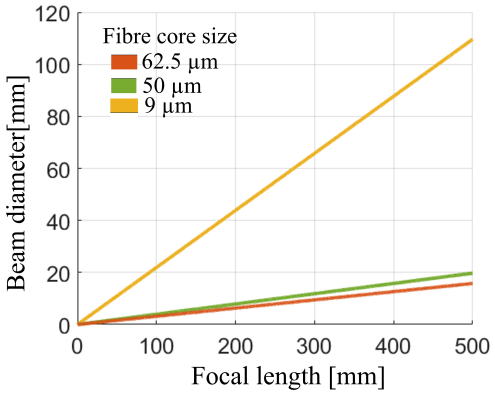


Figure 2.3: Collimated beam diameter at the transmit lens resulting from different focal lengths and fibre core sizes.

range from 30 mm to 300 mm. In this section, we discuss the use of these lenses with the standard telecommunication fibre cables in FSO systems.

When a light beam is launch out of a fibre cable, it diverges at an angle Θ given by Eq. 2.8. To channel it through the FSO link with narrow beam divergence, a transmitting lens is used to collimate the beam. The size of the collimated beam launched into the FSO link is dependent on the fibre core size and lens focal length, as the beam will diverge from the tip of the fibre till the lens. The radius of the collimated beam ω_{col} given as a function of the fibre core radius ω_{core} and lens focal length f as [49]

$$\omega_{col} = f\Theta = \frac{f\lambda}{\pi\omega_{core}}, \tag{2.13}$$

Fig 2.3 shows the collimated beam diameter of beams launch from the standard core size using lenses of different focal lengths. It should be noted that the smallest fibre core results in the largest beam diameter.

As mentioned in Sec. 2.2, the boundaries of a Gaussian beam are infinite. Therefore, only a portion of the power is transmitted through a finite circular aperture such as a lens. The power transmitted through a circular aperture of radius r is given by [50]

$$P = P_0 \left[1 - \exp\left(\frac{-2r^2}{\omega^2(z)}\right)\right], \tag{2.14}$$

where P_0 is the total power of the beam and is a function of the peak intensity (I_{peak}):

$$P_0 = \frac{\pi\omega_0^2 I_{\text{peak}}}{2}. \tag{2.15}$$

The percentage of optical power transmitted through a lens at various ratios of beam to lens radii is shown in Fig. 2.4. If the beam and lens radii are equal, only 86.5% of power is transmitted through the lens. The diameter of the lens used should be at least π times the radius of the beam to allow over 99% of the power through it. This is known as the "$D = \pi\omega$" or 99% criterion.

The size of the beam at the transmitter affects the amount of divergence experienced during propagation. It is necessary to design a transmitter that minimises divergence loss at the receiver. Fig. 2.5 shows the beam size along the propagation lengths when it is collimated at different sizes.

At the receiver side, the larger diverged beam will cause power loss, as less power will pass through the receiver. Fig. 2.4 shows that only 40% of the total power will pass through

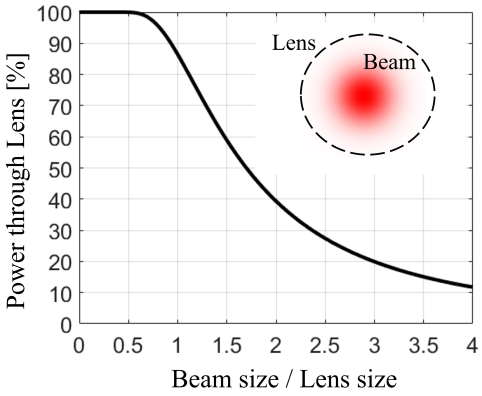


Figure 2.4: The power through a circular aperture. Only 86.5% of a beam's total power passes through a lens with a radius equal to its beam waist.

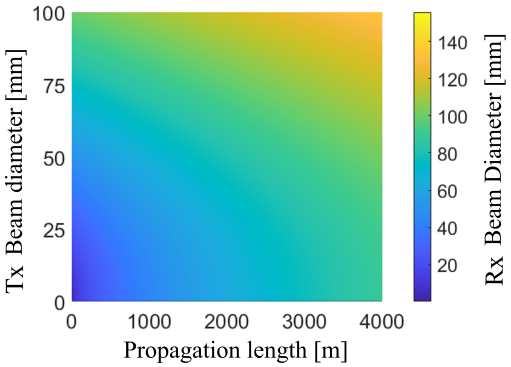


Figure 2.5: Resultant Beam size along propagation caused by different initial beam sizes at the transmitter. The beam diameter at the transmitter is represented on the Y-axis, while the diameter at the receiver is shown using the heatmap.

a lens if the beam is twice its size, and only 10% is received if the beam is four times larger than the lens. For this reason, it is advantageous to choose a receive lens large enough to match or exceed the expected beam size, optimizing power reception

Two important parameters to consider during fibre coming are numerical aperture of the incoming beam and the size of the focal beam spot, both of which are determined by the receiving lens. The radius of the focal beam spot can be regarded as the reverse of Eq. 2.13 to give

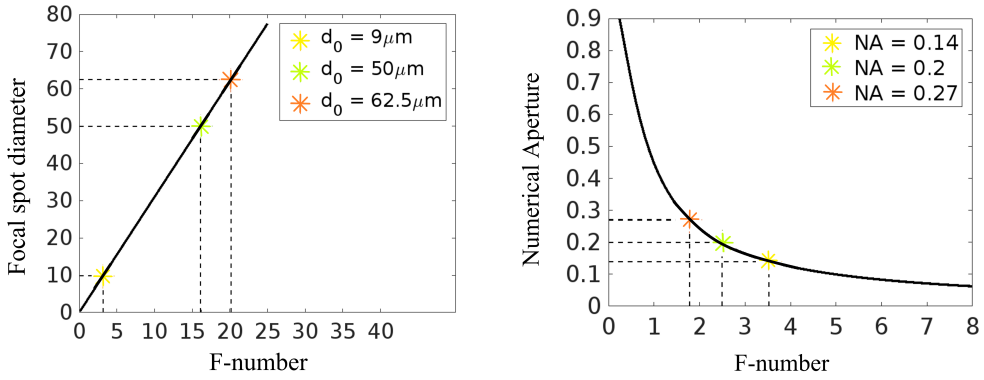
$$\omega_{focal} = \frac{\lambda f}{\pi \omega(z)}, \tag{2.16}$$

where $\omega(z)$ and ω_{focal} are the beam radii at the lens position along the propagation and at the lens focal point. Assuming the the "$D = \pi\omega$" criterion is adopted for the receiving lens, the focal spot diameter ($d_0 = 2\omega_{focal}$) is given as a function of the lens diameter as

$$d_0 = 2\lambda \frac{f}{D}. \tag{2.17}$$

Here, 86% of the total power is focused within d_0. The f-number (also known as the relative aperture or speed of the lens) is the ratio of the focal length and lens diameter ($f^{\#} = f/D$). Describing the focal spot diameter in terms of the f-number gives

$$d_0 = 2\lambda f^{\#}. \tag{2.18}$$



(a) Focal spot size

(b) Numerical Aperture

Figure 2.6: Focal spot diameter (a) and lens numerical aperture (b) resulting from different focusing lens f-numbers. Parameters of standard fibre cables are represented using the asterisks. The yellow asterisk represents the single-mode fibre, the green asterisk represents the OM2 to OM5 multi-mode fibres, and the red asterisk represents the OM1 fibre cable.

Focal beam spot diameters which results from different f-number values are shown in Fig. 2.6(a).

The numerical aperture of a lens is determined by its diameter and focal length. Lenses with large diameters and short focal lengths have high numerical apertures while small diameters and long focal lengths result in low numerical apertures. This relation is expressed as

$$\mathrm{NA} = \sin\left(\tan^{-1}\left(\frac{D}{2f}\right)\right) \approx \frac{1}{2f^{\#}}. \tag{2.19}$$

From this, it can be seen that the NA and f-number have an inverse proportional relationship. Fig 2.6(b) shows the resulting NA from different f-numbers.

Achieving optimal fibre coupling involves aligning the numerical aperture (NA) of the focusing lens with or below that of the fibre cable [34]. If the NA of the optics is too low, coupling efficiency decreases due to an increase in the focal beam spot size. For OM1 fibre cables with a numerical aperture of 0.27, an f-number of 1.78 or higher ensures an NA equal to or smaller than 0.27. A larger f-number, like 20.16, results in a focal spot size equal to the core size of 62.5 μm. In the case of OM2 to OM5 fibre cables, featuring NAs of 0.2 and a core size of 50 μm, the ideal f-number matching the NA is 2.45. An f-number of 16.13 yields a focal spot size equal to the core size. For single-mode fibres with an NA of 0.14 and a core diameter of 9.8 μm, an f-number of 3.54 matches the NA but results in a focal spot size exceeding the core size, leading to power loss. Achieving a focal spot size equal to the core size exceeds the fibre NA.

The above details the reception of a Gaussian beam. However, the minimum focal spot size achievable by an overfilled lens with uniform intensity is expressed as

$$\phi = 2.44\lambda f / D, \tag{2.20}$$

which is derived from the diffraction limit [51].

2.4 Effects of atmospheric turbulence on optical signals

Atmospheric turbulence is a significant challenge for FSO communication [52, 53]. It occurs due to random fluctuations in air temperature and pressure, which lead to the formation

of unstable air pockets known as turbulent eddies. These eddies create variations in the refractive index of the atmosphere, therefore affecting the transmission of optical beams. Large turbulent eddies break into smaller entities, forming an inertial sub-range. The largest turbulent cells are known as the outer scale eddies (L_0), and the smallest are known as the inner scale eddies (l_0). The strength of atmospheric turbulence can be characterized by a term known as the refractive index structure parameter (C_n^2). This term can be described by the Hufnagel-Valley model, which expresses it as a function of the altitude h to give [12]'

$$C_n^2(h) = 0.00594\left(\frac{V_{wind}}{27}\right)^2(10^{-5}h)^{10}\exp\left(-\frac{h}{1000}\right) + 2.7\times10^{-16}\exp\left(-\frac{h}{1500}\right) + A_0\exp\left(-\frac{h}{100}\right). \tag{2.21}$$

Here, V_{wind} is the wind speed and A_0 is the refractive index parameter at ground level[11]. Temperature variations are much greater at lower altitudes closer to the ground, leading to higher C_n^2 values at lower altitudes. For horizontal propagation paths, C_n^2 can be assumed to be constant [54]. Values of C_n^2 typically range from $10^{-17}m^{-2/3}$ in weak turbulence to $10^{-13}m^{-2/3}$ in strong turbulence [55]. The effects of atmospheric turbulence on propagating light signals include; beam wander, beam spreading, loss of spatial coherence, and scintillation. The extent of these effects is determined by the turbulence strength and propagation length.

2.4.1 Loss of spatial coherence

When a light beam travels through eddies smaller than its diameter, a portion of the light is deflected away from the rest of the beam, causing beam spreading and spatial incoherence. This leads to the blurring of optical signals and loss in the received power. The coherence length, also known as the Fried parameter, is the length in which the atmospheric turbulence is correlated. Within this length, the effects of turbulence are connected and predictable, while beyond this, turbulence is uncorrelated and independent [55]. The coherence length is a function of the refractive index parameter and propagation length L. It is calculated as

$$r_0 = 1.68\left(C_n^2Lk^2\right)^{-3/5}, \tag{2.22}$$

where k is the spatial frequency or wave number ($k = 2\pi/\lambda$).

For a uniformly distributed plane wave in a perfect optical collection system, the focal spot size in the focal plane a receiving lens is given by Eq. 2.20. However, when the light beam has propagated through the atmosphere, the receiver aperture is replaced by the coherence length r_0 to give a focal spot size of

$$\phi = 2.44\lambda F/r_0. \tag{2.23}$$

This implies that the focal spot size increases by a factor of D/r_0 in turbulence [51]. Turbulence induced beam spreading can be minimised by ensuring that the beam diameter is smaller than the coherence length of the atmosphere [12].

2.4.2 Beam wander and angle-of-arrival fluctuations

Beam wander refers to the bending of the light beam as it travels through turbulent eddies of varying refractive indices, creating a spiral motion through the atmosphere. This results in the lateral displacement and angle of arrival fluctuations at the receiving aperture, leading to misalignment in the focal plane. In case of a fibre-based receiver, such misalignment leads to power attenuation and signal fading. Turbulence induced beam wander is characterised by a long term average radial variance, $\langle r_c^2\rangle$, which is the radial variance of the beam's position.

For a collimated light beam with a radius of ω_0, average radial variance at a distance L along the propagation path is calculated as

$$\langle r_C^2 \rangle = 2.42 C_n^2 L^3 \omega_0^{-1/3}. \tag{2.24}$$

The radius in which the beam wanders at the receiver ω_{LT} (also known as the long-term beam size) can be calculated from the average radial variance and the instantaneous beam radius ω_{ST} (also known as short-term beam size) as

$$\omega_{LT}^2 = \omega_{ST}^2 + \langle r_C^2 \rangle, \tag{2.25}$$

The position of instantaneous beam typically follows a Gaussian shape within this long term beam diameter [55].

Turbulence-induced beam wander results in fluctuations in the Angle-of-arrival (AoA) at the receiver, which results in tilt misalignment on the detector. The variance is fluctuation of the angle-of-arrival $\langle \beta_a^2 \rangle$ is given by

$$\langle \beta_a^2 \rangle = 2.91 C_n^2 L (2\omega_G)^{-1/3}, \tag{2.26}$$

where ω_G is the radius of the receiving aperture.

2.4.3 Intensity fluctuations

If a turbulent eddy is of a similar size to the beam diameter, it focuses or defocuses the light in a lens-like manner. This leads to fluctuations in the light intensity detected at the receiving plane, which is known as scintillation. Scintillation often leads to degradation of the signal-to-noise ratio and deep signal fades. The amount of scintillation faced by an optical system is characterised using the normalized intensity variance of which is known as the scintillation index, σ_I^2. The scintillation index is calculated as

$$\sigma_I^2 = \frac{\langle I^2 \rangle - \langle I \rangle^2}{\langle I \rangle^2} = \frac{\langle I^2 \rangle}{\langle I \rangle^2} - 1, \tag{2.27}$$

where $\langle \cdot \rangle$ denotes the ensemble average and I represents the intensity.

In an experimental setting, fluctuations in intensity can be observed through the Strehl ratio, which is the ratio of the on-axis intensity in the presence of turbulence to the intensity in its absence. The Strehl ratio can be approximated as a function of the receive aperture D and r_0 as [56]:

$$SR = \frac{\langle I(0,L) \rangle}{I^0(0,L)} \approx \frac{1}{\left[1 + (D/r_0)^{5/3}\right]^{6/5}}. \tag{2.28}$$

Statistical approaches have been developed to describe the spatial power spectral density of atmospheric turbulence. These include models such as Tatarskii and von Karman spectrums. The most well-known expression is the Kolmogorov power-law spectrum which describes the power spectrum in the inertial sub-range. This model is expressed in terms of the vector wave number $\mathbf{k} = (k_x, k_y, k_z)$ as [56]:

$$\Phi_n(\mathbf{k}) = 0.033 C_n^2 \mathbf{k}^{-11/3}, \tag{2.29}$$

Mathematical models have also been utilised to characterise the probability density function (PDF) of random intensity fluctuations in turbulent conditions. The Log-Normal model is suitable for weak turbulence scenarios ($\sigma_I^2 < 1$) and is defined by the following PDF [57]:

$$f(I) = \frac{1}{I\xi\sqrt{2\pi}} \exp\left[-\frac{(\ln(I) - \mu)^2}{2\xi^2} \right], \tag{2.30}$$

where $\mu = \ln\left(\frac{\langle I\rangle}{\sqrt{1+\sigma_I^2}}\right)$ and $\xi^2 = \ln(1+\sigma_I^2)$.

On the other hand, the Gamma-Gamma statistical model accommodates turbulence across various regimes, accounting for both small and large-scale eddies through shape parameters α and β. The corresponding PDF, defined for $I > 0$, is given by:

$$f(I) = \frac{2(\alpha\beta)^{\frac{\alpha+\beta}{2}}}{\Gamma(\alpha)\Gamma(\beta)} I^{\left(\frac{\alpha+\beta}{2}\right)-1} K_{\alpha-\beta}(2\sqrt{\alpha\beta I}), \tag{2.31}$$

where $K_n(\cdot)$ is the modified Bessel function of the second kind of order n, and $\Gamma(\cdot)$ is the gamma function. The scintillation index σ_I^2 is interconnected with the shape parameters α and β through the relationship [58]:

$$\sigma_I^2 = \frac{1}{\alpha} + \frac{1}{\beta} + \frac{1}{\alpha\beta}. \tag{2.32}$$

Other statistical models found in literature include the negative exponential, log-normal, and M-generalized models. These models provide valuable tools for understanding and quantifying the impact of turbulence on optical signal characteristics.

2.5 Summary

This chapter aimed to highlight various factors influencing fibre-based FSO communication, a crucial foundation for understanding the work presented in this dissertation. We began by delving into the fundamental working principles of fibre cables and introduced the standard telecommunication fibre cables as defined by the international standard ISO/IEC 11801 of Information Technology. We then explored the propagation of Gaussian beams, emphasising how these beams diverge in the atmosphere. Additionally, we looked at how lenses, used to collimate light from the transmitting fibre and focus it onto the receiving fibre, influence the received power. Finally, atmospheric turbulence and its effects on propagating light beams, including phenomena such as beam wander, loss of spatial coherence, and scintillation, were discussed.

CHAPTER 3

Transmitter characterisation

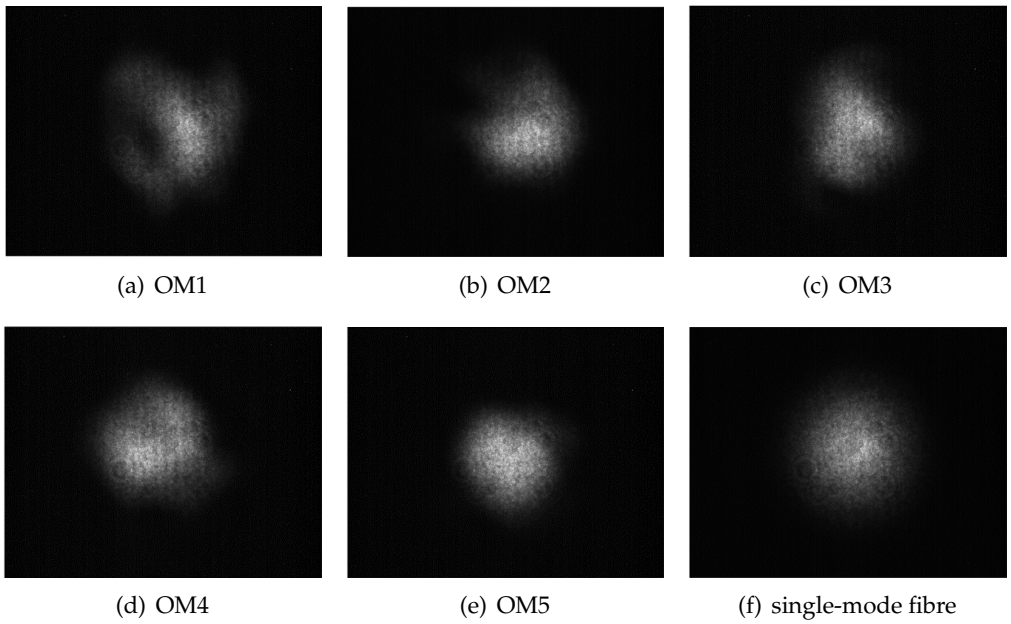
Transmission of light signals in the atmosphere is often influenced by various limiting factors, as detailed in Chapter 2. Therefore, ensuring the transmission of high power in the optimum spatial mode is crucial for Free Space Optical (FSO) communication, as it maximises the optical power reaching the receiver. Utilising the lowest order or fundamental Gaussian mode (TEM_{00}) proves advantageous for this purpose. This mode demonstrates reduced divergence compared to higher-order modes, enabling higher power density over extended propagation distances. Furthermore, the fundamental mode produces the smallest focal spot size characterised by a uniform Gaussian profile, making it suitable for fibre coupling [59].

Gaussian mode transmission can be achieved by launching light from a single-mode fibre cable, which is designed to transmit light in the fundamental mode [60]. However, this is not the case when transmitting from multi-mode fibres which are susceptible to mode coupling. Mode coupling refers to the transfer of power amongst different guided modes. This is caused by perturbations in the refractive index of the fibre cable. Such perturbations could be a result of bending or curving of the fibre cable as well as manufacturing imperfections [40]. Additionally, bending of the fibre cable results in the dissipation of optical power into the fibre cladding, which is referred to as bending loss [61].

For this reason, a Gaussian beam launched into a multi-mode fibre cable does not necessarily translate to a Gaussian beam emerging out of the fibre. Externally induced deformations cause mode coupling from the fundamental mode towards higher order modes, which diverge more in free space [62]. The extent of mode coupling varies amongst different fibre cables. It depends on different factors including propagation constants and physical dimensions. Furthermore, mode coupling is worsened in longer fibre cables [63] and is more prevalent in step-index fibre than in graded-index fibres [64].

Mode coupling causes distortion in the wavefronts of the optical fields emitted from the fibre cables. Examples of such distortion are shown in Fig. 3.1, where the intensity patterns of fields emitted from the standard fibre cables are presented. The field launched from the single-mode fibre is seen to have the most Gaussian shape.

This chapter characterises the transmission performance of telecommunication fibre cables by determining the optical power transmitted in the Gaussian mode. Modal decomposition is employed to analyse the modal content of fields launched from the fibre cables. Two SFP transceivers, labelled SFP A and B, are consecutively used as the light source. They operate at a wavelength of 1550 nm, have a power output rating of 1 mW, and have ranges of 120 km and 80 km, respectively. It should be noted that SFP A costs



(a) OM1 (b) OM2 (c) OM3

(d) OM4 (e) OM5 (f) single-mode fibre

Figure 3.1: Intensity images of beams launched from fibres cables when connected to an Small Form-factor Pluggable (SFP) transceiver module.

significantly more than SFP B. The testing of these transceivers aims to demonstrate that despite sharing the same power rating, such devices can exhibit variations. While literature as shown that graded-index fibres are less prone to mode coupling [64], we hypothesise that multi-mode fibre cables of higher modal bandwidth, indicative of their graded index profiles, will contain higher Gaussian mode content.

3.1 Transmitted optical power

The successful operation of an FSO link under the attenuating factors within the atmospheric channel requires high initial power at the transmitter. Therefore, to characterise the transmit performance of the different fibre cables, we first measure the optical power they transmit from the SFP transceivers. The rated power of the SFP transceivers is specified under the use of a single-mode fibre. Thus, it is necessary to measure how much power they transmit through larger multi-mode fibres.

The transmitted optical power is directly measured using a 1550 nm optical power meter. The fibre cables are successively connected to the SFP transceivers and optical power meter as seen in Fig. 3.2. The optical power was continuously measured for 30 seconds, while external deformations were exerted on the fibre cables. The external manipulation was done to induce mode coupling and bending losses. Inducing these losses in the measurements accounts for different orientations of the fibre cables, allowing for accurate measurements of transmitted power.

The average power measurements of each fibre cable were normalized by the average power transmitted through the single-mode fibre cable. Doing this shows how much more power the SFP modules transmit through multi-mode fibre cables relative to their rated power through a single-mode fibre. The normalized average power of each fibre cable is depicted in Fig. 3.3. These results reveal that the larger multi-mode fibre cables transmitted higher optical power than the single-mode fibre, with the highest power being transmitted by the OM1 fibre cable.

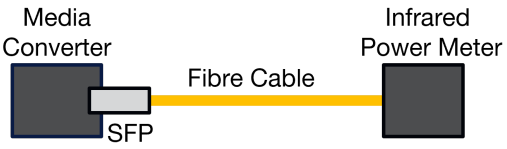
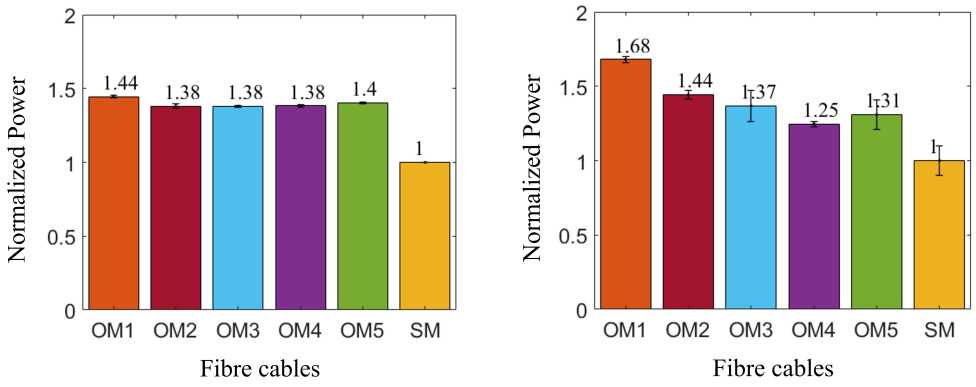


Figure 3.2: Experimental setup to measure power transmitted from SFP transceivers through the standard fibre cables. The fibre cables are manipulated during testing to induce mode coupling and bending losses.



(a) SFP A (b) SFP B

Figure 3.3: Measurements of optical power transmitted through fibre cables when connected to two types of SFP transceiver modules labelled SFP A and B. The optical power is normalized to the power in the single-mode.

From the average optical power depicted in Fig. 3.3(a), the multi-mode fibre cables are seen to transmit comparable power when connected to SFP A, with the OM1 fibre cable having the highest average power at 1.44. The OM2-OM4 fibre cables exhibited power of 1.38, while the OM5 fibre cable recorded power of 1.4 relative to the single-mode. Minimal variance in the measurements as seen from the narrow error bars which represent standard deviation. This suggests that minimal bending losses were experienced when the fibre cables were connected to SFP A.

The highest optical power, of 1.68 relative to the single-mode fibre, was recorded when the OM1 fibre cable was connected to SFP B as shown in Fig. 3.3(b). The power transmitted by the other multi-mode fibre cables varied between 1.25 in the OM4 fibre and 1.44 in the OM2 fibre cable. The external manipulations of the fibre cables resulted in greater power fluctuations when transmitting from SFP B, as seen from the wider error bars in Fig. 3.3(b). These findings show that larger-dimension fibre cables transmit higher power when connected to SFP transceivers designed for single-mode fibres. The results also highlight differences in laser quality between the two tested SFP transceivers. Notably, the laser in SFP B has higher power than that in SFP A, enabling greater power transmission through the OM1 fibre cable. However, the observed fluctuation in transmitted power when manipulating the fibre cables with SFP B suggests an increased susceptibility to bending losses compared to SFP A. This indicates a higher presence of higher-order modes in the light emitted from SFP B compared to SFP A, as higher-order modes are more sensitive to bending and more prone to dissipation in the cladding [65]. This implies that the more expensive transceiver, SFP A, uses a higher-quality laser than the one in SFP B.

3.2 Modal decomposition of fields emitted from fibre cables

The Gaussian content emitted from the fibre cables is measured through a process known as modal decomposition. This works on the premise that all optical fields can be described as a superposition of weighted orthogonal basis functions(modes), allowing for their deconstruction into elementary units. Essentially, modal decomposition is the process of determining the weightings of each basis function. These are generally expressed as complex expansion coefficients. An arbitrary optical field, $U(\mathbf{x})$ can be expanded into a chosen basis $\Phi_n(\mathbf{x})$ as:

$$U(\mathbf{x}) = \sum_n C_n \Phi_n(\mathbf{x}), \tag{3.1}$$

where C_n is the complex expansion, n is the mode index and $\mathbf{x}$ the transverse spatial coordinates [66]. This decomposition can be performed by measuring the inner product of the arbitrary field and the conjugates of the basis functions [67]. The result of this overlap integral gives the mode weighting as

$$C_n = \langle \Phi_n | U(\mathbf{x}) \rangle = \int \Phi_n^*(\mathbf{x}) \cdot U(\mathbf{x}) \mathrm{d}^2\mathbf{x}. \tag{3.2}$$

This overlap integral can be performed optically by projecting the field of interest onto a Spatial Light Modulator (SLM), where the conjugates of the basis modes are successively encoded [68]. Therefore, the encoded transfer function would be

$$T(\mathbf{x}) = \Phi_n^*(\mathbf{x}). \tag{3.3}$$

A Fourier transform is then performed on the emerging beam by focusing it using a lens of focal length f. The wavefront at the focal point $W(\mathbf{k})$, is given in terms of the spatial frequency $\mathbf{k}$ as:

$$W(\mathbf{k}) = C \int_s \Phi_n^*(\mathbf{x}) U(\mathbf{x}) \cdot \exp\left(-i \frac{2\pi}{\lambda f} \mathbf{k} \cdot \mathbf{x}\right) \mathrm{d}^2\mathbf{x}. \tag{3.4}$$

With a detector at the focal point, the on-axis amplitude ($\mathbf{k} = 0$) can be observed which is expressed as

$$W(0) = C \int_s \Phi_n^*(\mathbf{x}) U(\mathbf{x}) \mathrm{d}^2\mathbf{x} \propto C_n. \tag{3.5}$$

This on-axis amplitude is proportional to the expansion coefficient of the corresponding basis mode.

Modal decomposition can be performed using any orthogonal basis, including Orbital Angular Momentum (OAM) modes [67, 69]. OAM is a property of light seen in waves which have a helical phase with a singularity in the centre. This causes the waves to propagate in a twisted form with zero amplitude at the position of the singularity. Several beams exhibit this vortex behaviour. with the most widely known being the Laguerre Gaussian (LG) beams. The complex distribution of an LG beam at the beam waist (ω_0) is described in its cylindrical coordinates as

$$\mathrm{LG}_p^\ell(\mathbf{r}, \theta) = \sqrt{\frac{2p!}{\pi \omega_0^2 (p + |\ell|)!}} \left[\frac{\mathbf{r}\sqrt{2}}{\omega_0}\right]^{|\ell|} \mathrm{L}_p^{|\ell|}\left(\frac{2\mathbf{r}^2}{\omega_0^2}\right) \exp\left[\frac{-\mathbf{r}^2}{\omega_0^2}\right] \exp(i\ell\theta). \tag{3.6}$$

Where $\mathbf{r}$ and θ are the radius vector and transverse azimuthal angle, $L_p^{|\ell|}(\cdot)$ is the corresponding Laguerre polynomial and the two indices p and are the radial index and azimuthal index. The helical phase, which characterizes the OAM, is described in the term $\exp(i\theta)$. Thus, is also known as the OAM mode index. Setting the radial index p to zero in equation 3.6, gives an orthogonal OAM basis, allowing for a modal decomposition of a field as

$$U(\mathbf{r}, \theta) = \sum C_\ell \mathrm{LG}_0^\ell(\mathbf{r}, \theta). \tag{3.7}$$

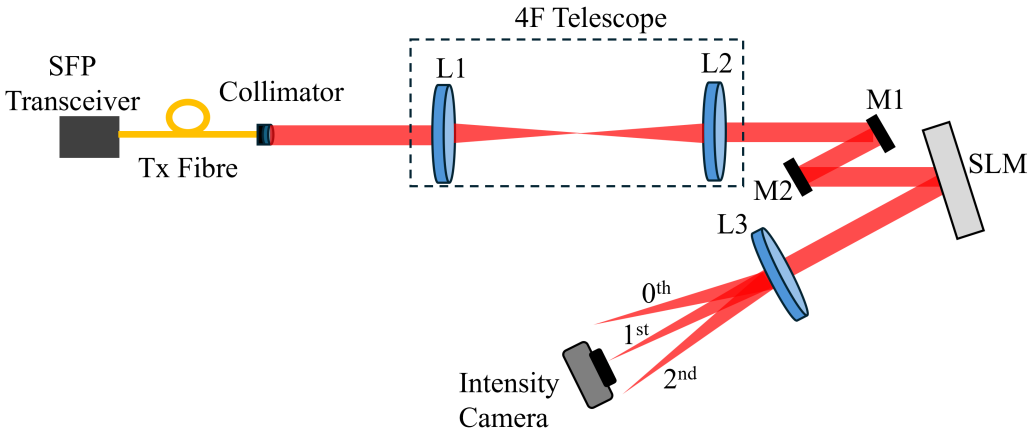


Figure 3.4: Experimental setup to perform modal decomposition of fields launched by fibre cables, represented as Tx Fibre. Lenses L1 and L2 are used as a 4F telescope, which mirrors M1 and M2 are used to align the beam to the SLM. Lens L3 performs a Fourier transform on the beam and separates the diffraction orders (0^{th}, 1^{st} and 2^{nd}). The 1^{st} diffraction order is observed with an intensity camera.

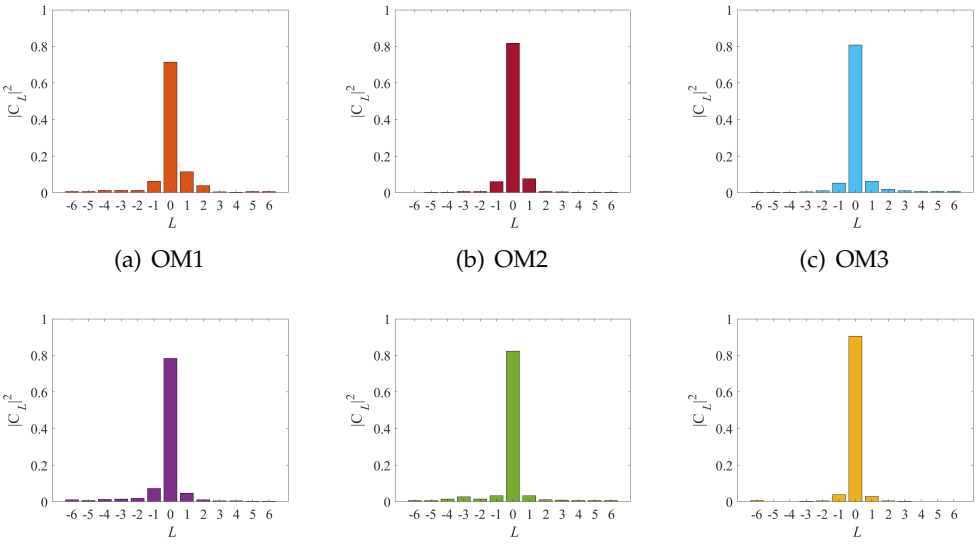
3.2.1 Experimental setup to conduct modal decomposition

The experimental setup used to perform the modal decomposition is shown in Fig. 3.4. In this setup, the fibre cable being assessed is connected to an SFP transceiver, which is used as the 1550 nm light source. The two transceivers, SFP A and SFP B, are successively tested. The light beam emerging from the fibre cable is collimated using a fibre collimator with a focal length of 37.13 mm. A 4f-telescope, formed by lenses L1 and L2, is added to the beam path to relay (or image) the beam from the fibre collimator to the SLM screen. This telescope has a unity magnification and is added to the setup to avoid unnecessary divergence of the beam. Two mirrors (M1 and M2) are placed in the beam path to ensure that the centres of the beam and SLM align.

The conjugate phase profiles of 13 OAM modes ($\ell = -6$ to $\ell = 6$) are successively encoded onto the SLM as the transmission function. The phase of a diffraction grating is added to the transmission function to separate modulated and un-modulated light. Lens L3, of 200 mm focal length, is used to perform the overlap integral of the resultant beam emitting from the SLM. At the focal point, the diffraction orders are physically separated, with the unmodulated light focusing in the zero order beam. A CCD camera is placed at the focus of the first order beam, which has the highest modulated intensity. Here, the central intensity measured, which is proportional to the modal expansion coefficient as expressed in Eq. 3.5.

The CCD camera used is a near infrared camera with a resolution of 1296 by 964 pixels. Each pixel measures 3.75 μm in size, with bit depth of up to 16 bit. To minimize noise, the highest bit depth is used, which maximize the dynamic range and Signal to noise ratio (SNR). The shutter time is optimized to ensure high SNR while avoiding saturation [66]. Furthermore, 30 frames were captured and averaged per trigger to minimize noise, and minimal gain was used, to preserve the accuracy the measurements.

The centre of the image captured by the CCD camera is determined by calculating the centre of mass. In mechanics, the centre of mass is a point on an object where a single force can be applied to represent all gravitational forces exerted on the object. This can be done in image processing by regarding the intensity incident on each pixel as a mass [70]. For a two dimensional image, the x and y pixel position (x_{COM}, y_{COM}) of the centre of mass is given



(a) OM1 (b) OM2 (c) OM3

(d) OM4 (e) OM5 (f) single-mode fibre

Figure 3.5: Average modal content of beams from SFP A. The modal content was averaged across 5 measurements. All fibre cables exhibited high Gaussian content.

by

$$x_{COM} = \frac{\sum_x \sum_y xI(x,y)}{\sum_x \sum_y I(x,y)} \tag{3.8}$$

$$y_{COM} = \frac{\sum_x \sum_y yI(x,y)}{\sum_x \sum_y I(x,y)}. \tag{3.9}$$

Here $I(x,y)$ is the intensity on the corresponding pixel.

However, this single pixel representing the centre of mass can not be used accurately as the centre of the beam, as it is susceptible to noise. Instead, the minimum resolvable diameter given by the Rayleigh criterion was used as the central region, around the centre of mass. The number of pixels across the diameter of the central region is calculated as

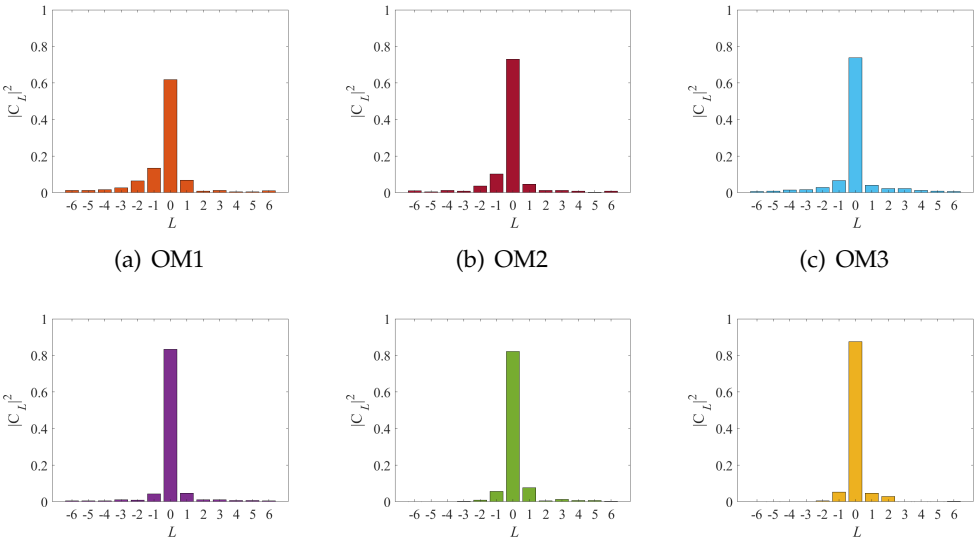
$$\text{No. of Pixels} = 2.44\frac{\lambda f}{D} \times \frac{1}{\text{Pixel Size}}. \tag{3.10}$$

For a focal length f of 200 mm and an aperture D of 10.8 mm (corresponding to the SLM dimensions of 14.4 mm by 10.8 mm), the number pixels within the diameter of the central region is 18.68. The total intensity in this region was measured, resulting in a value proportional to the mode weighting coefficient.

To confirm the validity of this modal decomposition, 5 measurements were taken for each orthogonal base as was performed in Ref. [71]. The fibre cables were bent into different positions for each measurement to encourage mode coupling and obtain realistic results. Positions yielding high horizontally polarized beams were preferred as they resulted in higher power modulated by the SLM.

3.2.2 Results and discussion

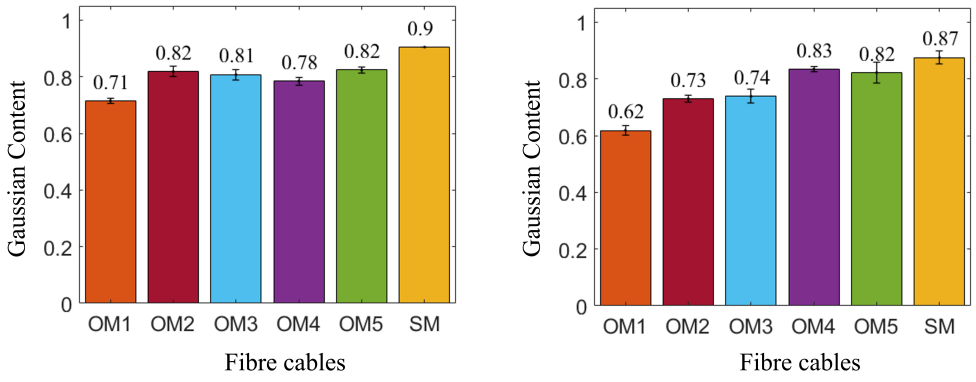
The procedure of modal decomposition explained above was performed on the optical fields launched out of the fibre cables when connected to the two SFP transceiver modules. The weighting coefficients corresponding to each of the 13 OAM modes was normalized



(a) OM1 (b) OM2 (c) OM3

(d) OM4 (e) OM5 (f) single-mode fibre

Figure 3.6: Average modal content of beams from SFP B. The modal content was averaged across 5 measurements. All fibre cables exhibited high Gaussian content.

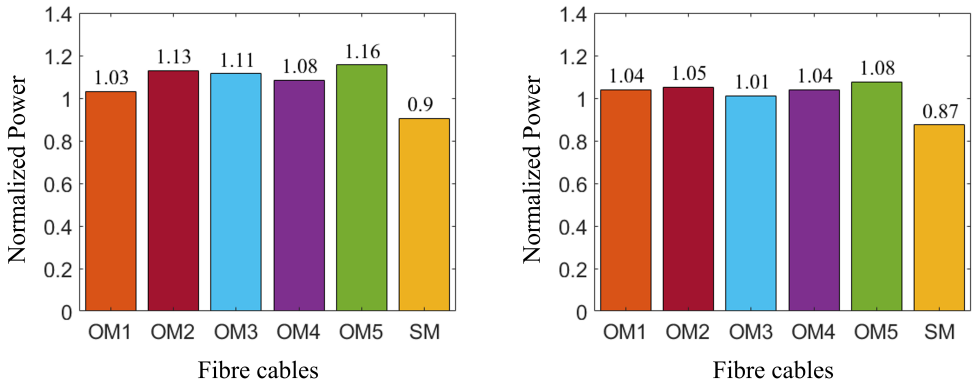


(a) SFP A (b) SFP B

Figure 3.7: Average Gaussian content measured from fields launched out of the fibre cables. The single-mode fibre, represented by SM, records the highest Gaussian content.

to their sum, giving an indication of the amount each mode represented in the total field. The average normalized weighting coefficients from the 5 measurements taken for each fibre are shown in Fig. 3.5 and Fig. 3.6 when connected to SFP A and B respectively. These measurements display a high Gaussian content in all fields, with the highest cross talk amongst the modes adjacent to the Gaussian mode ($\ell = 1$ and $\ell = -1$). High Gaussian content is expected as the SFP transceivers are designed to transmit signals through a single-mode fibre. Furthermore, the standard fibre cables all have graded index cores, making the more resilient to mode coupling [64].

However, the Gaussian content transmitted through the fibre cables is not equal. Fig. 3.7 shows the normalized Gaussian content transmitted through the fibre cables when connected to the SFP transceivers. As expected, the single-mode fibre cable exhibits the the highest Gaussian content, with 0.9 from SFP A and 0.87 from SFP B. Noise and imperfections within



(a) SFP A (b) SFP B

Figure 3.8: Product of average Gaussian content and normalized optical power relative to the power transmitted by the single-mode fibre cable. The OM5 fibre cable records the highest Gaussian power.

the modal decomposition set-up prevented the detection in the single-mode fibre from recording total Gaussian content. The OM1 fibre recorded the lowest Gaussian content from both transceivers with 0.71 in SFP A and 0.62 in SFP B. Having the largest core size, the OM1 fibre cable supports a highest number of modes amongst the fibre cables tested. Furthermore, being the earliest version of the multi-mode fibre tested, the OM1 fibre has the least graded index profile, as seen from it having the lowest modal bandwidth in Tab. 2.1. This all makes it more susceptible to mode coupling. Connecting the 50 μm core fibres (OM2 - OM5) to SFP A resulted in similar Gaussian content. However, when connected to SFP B, the Gaussian content in the OM4 and OM5 fibre cables was significantly higher compared to that in the OM2 and OM3 fibre cables. This suggests that the newer versions of multi-mode fibres, characterised by greater graded index profiles, maintain a higher degree of power in the fundamental Gaussian. Finally, The majority of fibre cables exhibited a higher Gaussian content when transmitting from SFP A compared to SFP B. This supports the initial assumption that SFP A incorporates a higher-quality laser than SFP B.

The normalized power transmitted in the Gaussian mode is determined by multiplying the average Gaussian content by the normalized power relative to the single-mode fibre cable. The results are depicted in Fig. 3.8. SFP A transmitted the highest power in the Gaussian mode across the fibre cables, despite the SFP B recording the highest optical power relative to the single-mode. The OM5 fibre cable demonstrated the highest transmission of Gaussian power from both transceivers, with 1.16 from SFP A and 1.08 from SFP B relative to the single-mode fibre. Intriguingly, despite the single-mode fibre cable exhibiting the highest Gaussian content, it recorded the lowest optical power from the transceivers, leading to the lowest Gaussian power transmitted.

3.3 Conclusion

In the context of fibre-based FSO communication, the transmission of light in Gaussian mode proves advantageous due to the diminished divergence experienced by these beams compared to higher-order beams. Additionally, Gaussian beams exhibit the smallest focal spot diameter. However, the transmission of a Gaussian beam from a multi-mode fibre is constrained by mode coupling, leading to power distribution to other guided modes. This chapter delved into the investigation of Gaussian content transmitted through standard fibre cables using modal decomposition. This process involved breaking down fields

emitted from the fibre cables into a series of OAM orthogonal modes. Light sources for this investigation were two types of SFP transceiver modules.

The investigation commenced by assessing the power channelled from the SFP transceivers through different fibre cables by directly measuring transmitted optical power using a power meter. Larger multi-mode fibre cables were found to channel more optical power from single-mode rated SFP transceivers, with the OM1 fibre cable transmitting optical power 1.68 times that of the power transmitted in the single-mode fibre when connected to SFP B.

The modal decomposition revealed a notable correlation between Gaussian content and the extent of the fibre's graded-index. Fibre cables with lower modal bandwidths, indicative of lower graded indices, demonstrated less Gaussian content compared to their newer counterparts characterised by higher modal bandwidths.

Discrepancies in Gaussian content and transmitted power between SFPs A and B were observed, indicating that SFP A transmitted a higher degree of Gaussian content than SFP B. The signal transmitted from SFP B was shown to be more prone to mode coupling and bend losses. This emphasises that SFP transceiver modules cannot be assumed to have the same performance in free space, despite having the same power rating through a single-mode fibre cable.

Finally, the Gaussian content in each fibre cable and the corresponding optical power relative to the single-mode fibre were multiplied to determine the Gaussian optical power transmitted by the fibre cables when connected to the SFP modules. The results indicated that the OM5 fibre cable transmitted the highest Gaussian power amongst the standard fibre cables tested with both SFP modules. Conversely, despite having the highest Gaussian content, the single-mode fibre transmitted the lowest Gaussian power due to the lower power it channels from an SFP module.

CHAPTER 4

Receiver characterisation

In the realm of fibre-based Free Space Optical (FSO) communication, the efficient coupling of light signals from free-space into the receiving fibre cable is a crucial prerequisite for reliable connection. Only the signals successfully coupled into the fibre cable can be directed to the detector for further processing. This principle holds true for FSO systems which utilise Small Form-factor Pluggable (SFP) transceivers, where optical signals are routed to the Receiver Optical Sub-Assembly (ROSA).

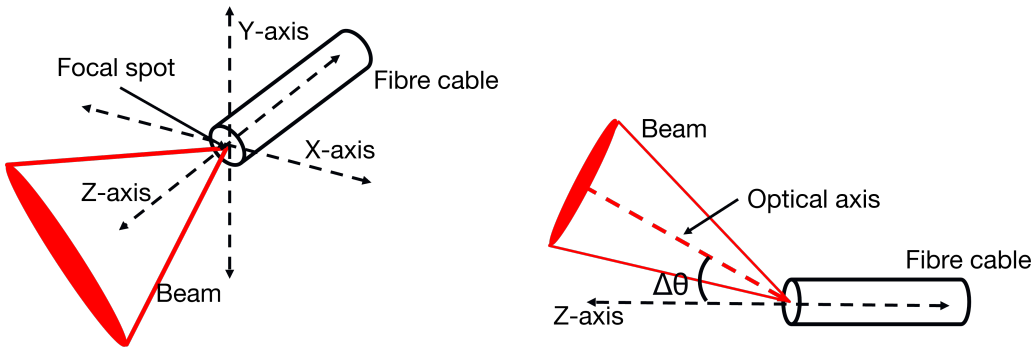
While successful free-space to fibre coupling relies on precise alignment, practical FSO systems face various challenges which result in misalignment. These sources of misalignment include fibre positioning error, vibrations and building sway [72]. Furthermore, the optical aberrations caused by atmospheric turbulence lead to inefficient fibre coupling [30, 31, 73, 74]. Thus, it becomes imperative to utilise fibre cables capable of maintaining high power coupling when faced with misalignment and atmospheric turbulence.

While previous studies have investigated the effects of misalignment and atmospheric turbulence on fibre coupling in various fibre types, such as single-mode fibre [75, 76] and few-mode fibres [29, 33], a comprehensive examination is necessary if generic telecommunication fibre cables standardised in ISO 11801-1:2017 [43] are to be employed for FSO applications.

This chapter focuses on the effects of misalignment and atmospheric turbulence on the optical power coupled into these telecommunication fibre cables. The chapter consists of two sections, with Sec. 4.1 focusing on fibre coupling under misalignment, and Sec. 4.2 addressing fibre coupling in the presence of simulated atmospheric turbulence. We hypothesise that the larger fibre cables, which support a higher number of modes, will show more resilience to the optical aberrations induced by turbulence.

4.1 Fibre coupling under misalignment

The ability of the standard fibre cables to couple light under misalignment was assessed by measuring the optical power coupled into them during experimentally induced misalignment. The study considered three forms of misalignment: lateral, angular and longitudinal misalignment [76, 77]. Lateral misalignment denotes the shift of the beam's focal spot along the x and y axes on the face of the fibre cable, illustrated in Fig. 4.1(a). Angular misalignment refers to the angular difference between the optical axis of the incoming beam and the longitudinal axis (z-axis) of the fibre cable, as depicted in Fig 4.1(b). Lastly, longitudinal misalignment pertains to the displacement of the focal spot along the longitudinal axis of the



(a) Fibre axes (b) Incoming angle

Figure 4.1: Cartesian axes on the tip of a fibre cable (a) and angular misalignment on an incoming beam (b).

fibre cable. Examining the optical power coupled under these diverse forms of misalignment facilitates a thorough analysis of the fibre cables' resilience to misalignment.

4.1.1 Experimental setups to test fibre coupling under misalignment

The experimental setup, illustrated in Fig. 4.2, was constructed to investigate the effects of focal point lateral and angular misalignment on fibre coupling. A 1550 nm infrared laser coupled with a single-mode fibre cable served as the light source. The use of a single-mode fibre ensured the generation of a Gaussian beam, which is well-suited for fibre coupling due to its high central intensity.

The beam undergoes collimation through a fibre collimator with a focal length of 15.58mm, resulting in an approximate beam waist of 1.71 mm. The beam waist (ω_{col}) is calculated using the formula:

$$\omega_{\text{col}} = \frac{f\lambda}{\pi\omega_{\text{fibre}}}, \tag{4.1}$$

where f is the focal length, λ is the wavelength, and ω_{fibre} is the fibre core radius of 4.5 μm. The collimated beam diameter, approximately twice the beam waist, is calculated to be 3.42 mm.

After collimation, the beam is directed towards the Spatial Light Modulator (SLM) using two mirrors, denoted as M1 and M2. These mirrors are positioned to ensure the beam propagates parallel to the optical table. To achieve the necessary expansion for overfilling the SLM screen, a 4f telescope, comprised of lenses L1 and L2, is employed. Lenses L1 and L2, with focal lengths of 50 mm and 300 mm, respectively, provide an expansion factor of 6. Consequently, the beam diameter is expanded to 20.52 mm, effectively overfilling the SLM screen, which has dimensions of 14.4 mm $\times$10.5 mm. This overfilling is crucial for the subsequent discussion on introducing tilt misalignment. A Gaussian phase with a 2.5 mm beam waist is encoded onto the SLM along with a diffraction grating as seen in Fig. 4.3(a).

The beam emerging from the SLM undergoes further manipulation in the optical setup. Lens L3, which has a focal length of 200 mm, is employed to focus the resultant beam and separate different diffraction orders in the Fourier plane. A pinhole aperture is strategically positioned to isolate the first order beam, while concurrently blocking other orders, including the zeroth order. The first order beam passes through the pinhole and is incident upon Lens L4, which has the same focal length as L3. This 4f arrangement effectively relays the first order beam from the SLM to the back focal length of L4. To facilitate alignment onto the fibre cables, two mirrors, M3 and M4, are placed along the propagation path after lens L4. Lens L5, with a diameter of 25.4 mm and focal length of 30 mm, is then introduced to focus

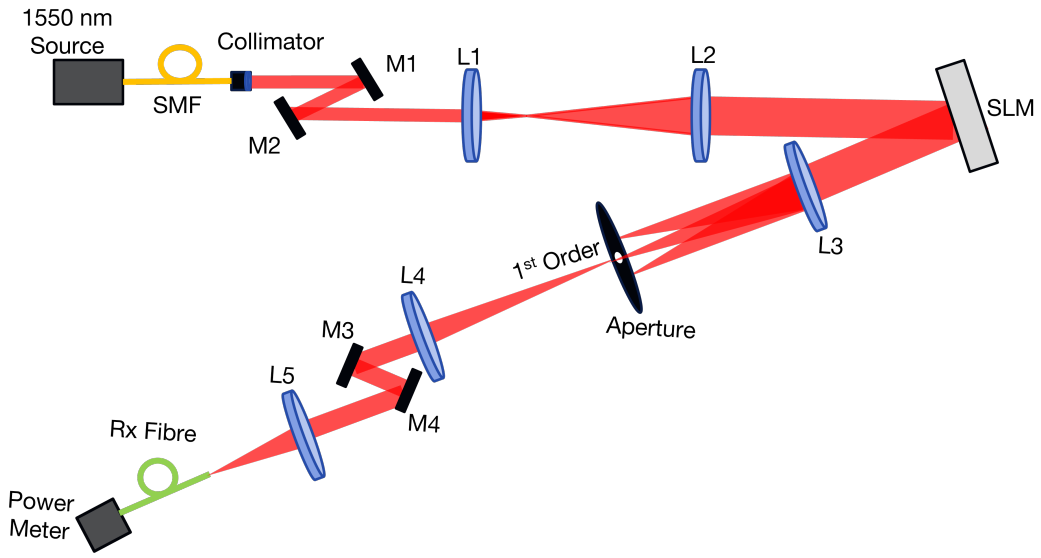


Figure 4.2: Experimental setup to observe the effects of lateral and angular misalignment on the power coupled into the standard fibre cables. SMF represents a single mode fibre while Rx Fibre represents the different fibre cables tested. M1, M2, M3 and M4 represent mirrors used for alignment. Lenses L1 and L2 of focal lengths 50 mm and 300 mm respectively, form a 4f expansion telescope system. Lenses L3 and L4 each have a focal length of 200 mm. Lens L5, with a focal length of 30 mm, focuses the beam onto the fibre cables.

the beam onto the fibre cables. These lens parameters result in a numerical aperture of 0.39 according to Eq. 2.19, and an approximated focal point beam diameter of 11.84μm for a 5mm collimated beam diameter according to Eq. 2.13. Placed at an optical path length of 230 mm away from lens L4 (the sum of their focal lengths), Lens L5 focuses the beam onto the fibre cables. An XY translation mount was used to optimise the lateral position of the fibre cables while a Z-axis mount was used to optimise the position of the lens and ensure that the fibre cable were at its focal point. The optical power coupled into the fibre cables is quantified using an infrared power meter, which has an optical power range of 50 nW to 40 mW and a resolution of 2 nW. Precise adjustments to mirrors M3 and M4 are meticulously made to maximize coupling efficiency before introducing any misalignment. The power measurements recorded during misalignment are normalized relative to the maximum power coupled into the fibre cables under the best achievable alignment conditions.

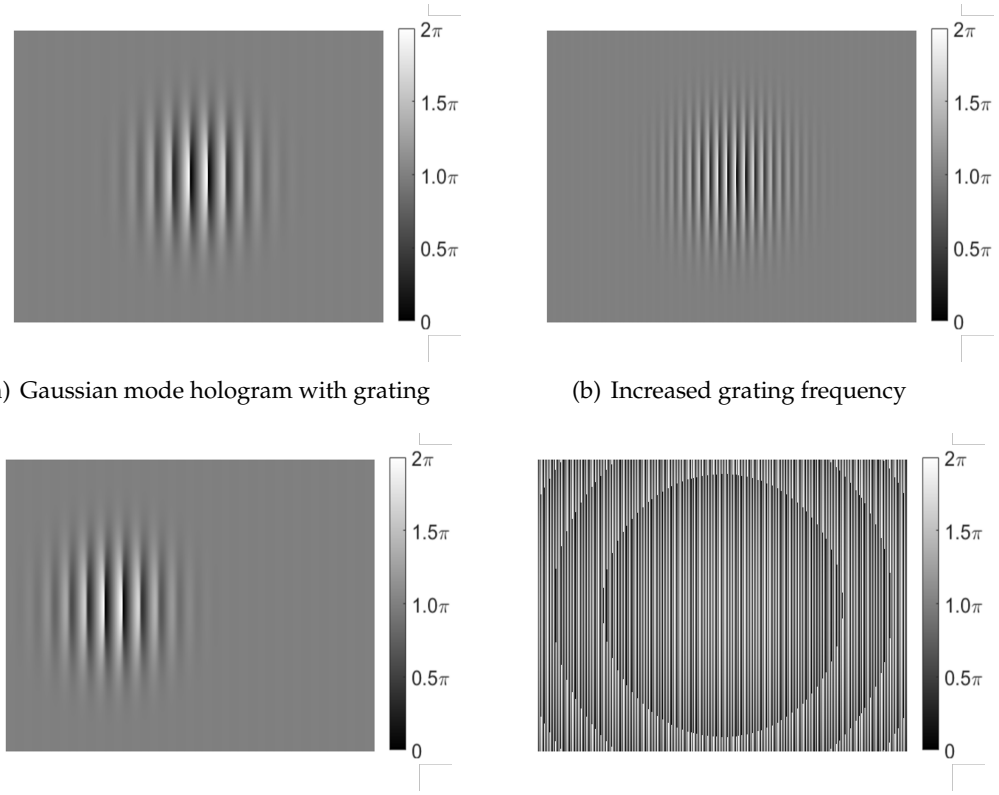
4.1.1.1 Lateral misalignment

The impact of lateral misalignment on the coupling performance of standard fibre cables was observed using the experimental setup depicted in Fig. 4.2. To induce lateral misalignment, the grating frequency of the encoded diffraction grating is manipulated, resulting in a change in the angle of the emerging first-order beam.

Alterations in the angle ($\Delta\beta$) at which the first-order beam is emitted from the SLM lead to a laterally displaced and tilted beam reaching lens L3, as illustrated in Fig. 4.4. The first-order beam then propagates parallel to the principal axis with a constant lateral displacement, ΔL, calculated by

$$\Delta L = \mathrm{F3}\tan(\Delta\beta). \tag{4.2}$$

The laterally displaced beam reaches lens L4, where it emerges as a tilted beam inter-



(a) Gaussian mode hologram with grating

(b) Increased grating frequency

(c) Shifted hologram

(d) Encoded lens

Figure 4.3: A Gaussian mode hologram and diffraction grating encoded on the SLM screen (a). The grating frequency is increased to change the angle of the first order beam in order to impose focal point lateral displacement (b). The hologram is shifted to laterally shift the first order beam and impose tilt misalignment (c). A Fourier lens is encoded onto the SLM to impose longitudinal misalignment (d).

secting the principal axis at the lens' focal point with a tilt angle, $\Delta\Phi$, calculated by

$$\Phi = \tan^{-1}\left(\frac{\Delta L}{\mathrm{F4}}\right). \tag{4.3}$$

The tilted beam then reaches the receiving lens L5 at a displacement Δd off the centre, resulting in a focal spot laterally displaced from the optical axis by Δd, calculated as

$$\Delta\mathrm{d} = \mathrm{F5}\tan(\Phi). \tag{4.4}$$

4.1.1.2 Angular misalignment

Angular misalignment in fibre coupling induces power loss as the angle of the incoming beam approaches the fibre acceptance angle, leading to dissipation within the cladding. To assess the impact of angular misalignment on fibre coupling, it was imposed on the standard fibre cables using the experimental setup in Fig. 4.2. The center of the encoded hologram was shifted across the SLM screen, causing a lateral shift in the first-order beam, denoted as ΔL. This shift resulted in a tilted beam emerging in the focal plane of lens L3, as depicted in Fig. 4.5. The beam intersected the principal axis at an angle Φ, calculated as

$$\Phi = \tan^{-1}\left(\frac{\Delta d}{\mathrm{F3}}\right). \tag{4.5}$$

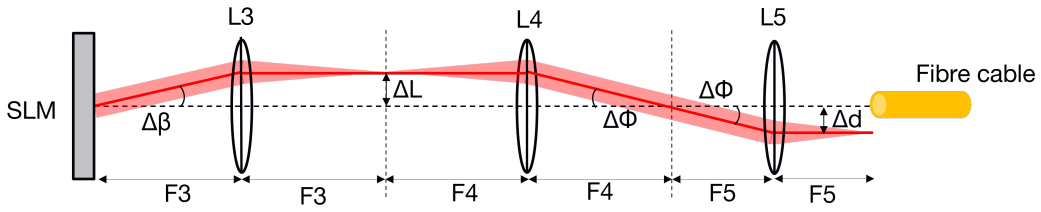


Figure 4.4: Application of lateral displacement on the fibre tip. This is achieved by manipulating the grating frequency encoded on the SLM, resulting in the angular change $\Delta\beta$. The lateral offset on the fibre tips is represented by Δd.

At this angle, the beam struck lens L4 at a distance ΔS away from the center, given by

$$\Delta S = \mathrm{F4}\tan(\Phi). \tag{4.6}$$

The displacements ΔL and ΔS are equal since lenses L3 and L4 share the same focal lengths.

The beam then reached lens L5 at the same displacement, resulting in an angle θ at the focal point. This angle represents the tilt misalignment on the fibre tip and is calculated as

$$\Delta\theta = \tan^{-1}\left(\frac{\Delta S}{\mathrm{F5}}\right). \tag{4.7}$$

The relationship between the position of the hologram on the SLM screen and the tilt angle is expressed as

$$\Delta\theta = \tan^{-1}\left(\frac{\mathrm{F4}}{\mathrm{F3}\times\mathrm{F5}}\Delta\mathrm{d}\right). \tag{4.8}$$

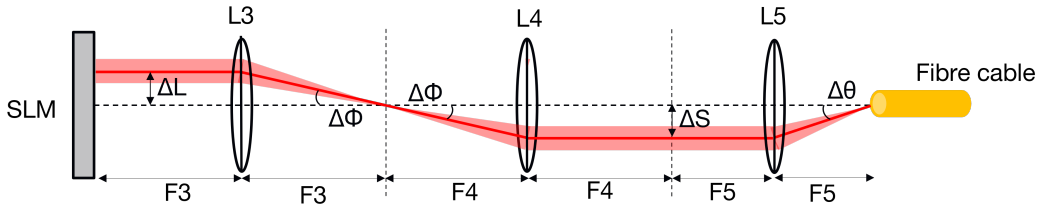


Figure 4.5: Application of angular misalignment on the fibre tip. This is achieved by laterally displacing the beam on the SLM screen by ΔL. The resulting angular offset at the fibre tip is given by $\Delta\theta$

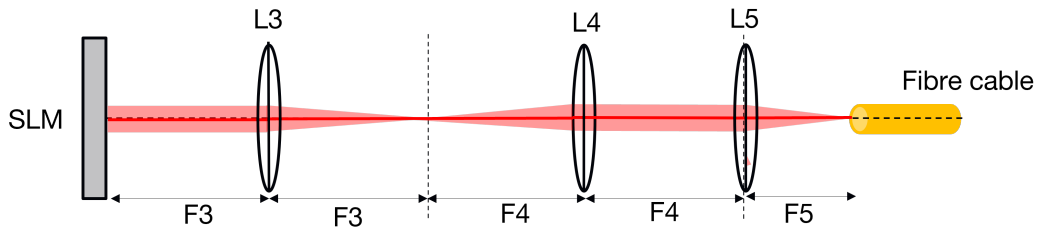


Figure 4.6: Application of longitudinal misalignment on the fibre cable. This is achieved by encoding a Fourier lens onto the SLM, which is then relayed onto the receiving lens L5. The encoded lens and lens L5 emulate a compound lens with a variable focal length.

4.1.1.3 Longitudinal misalignment

The effect of longitudinal misalignment was observed using the experimental set-up depicted in Fig. 4.2, with specific modifications. The 4f telescope consisting of Lenses L1 and L2 was removed to prevent overfilling the SLM. The transmission function on the SLM was then changed to an encoded Fourier lens and diffraction grating. Lens L5 was positioned at the back focal point of L4, establishing a 4F distance between L5 and the SLM. This arrangement directly relayed the SLM's image onto the receiving lens L5, effectively creating a compound lens system with the encoded lens and L5 behaving as two thin lenses in contact. Manipulating the encoded focal length allowed adjustments to the focal point of the compound lens, facilitating the imposition of longitudinal misalignment. The combined focal length is given by

$$\frac{1}{F_{com}} = \frac{1}{F_{SLM}} + \frac{1}{F5}, \tag{4.9}$$

where F_{SLM} represents the encoded focal length, and F5 is the length of the receiving lens.

4.1.2 Effect of misalignment on coupled power

The experimental setups described above were used to impose lateral, angular, and longitudinal misalignment on the standard fibre cables. The optical power coupled into each fibre cable was recorded under each form of misalignment and normalized relative to the maximum power coupled under the best alignment.

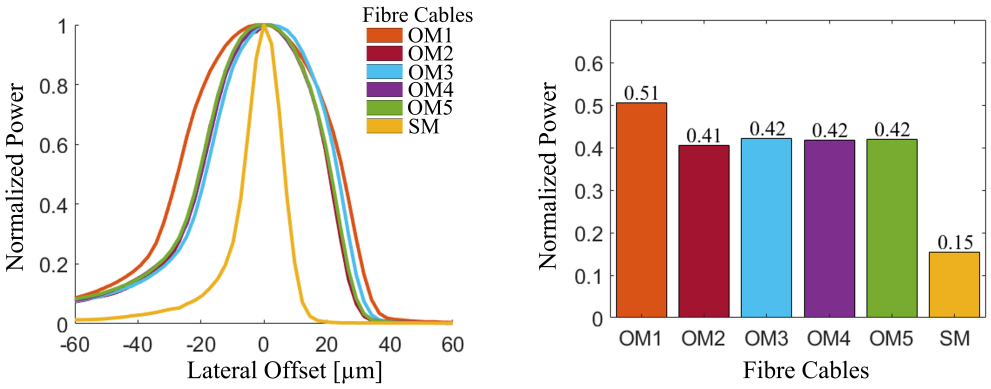
The lateral displacement of the beam spot from the fibre axis resulted in a loss of coupled power across all fibre cables. The focal beam spot underwent a lateral shift spanning 120 μm (from -60 μm to 60 μm). Within this range, the 62.5 μm, 50 μm, and 9 μm fibre core sizes represented 52%, 41.7%, and 7.5%, respectively. Notably, the single-mode fibre cable, featuring the smallest core size, exhibited the most significant power loss under lateral misalignment, with an average normalized power of 0.15 across the tested range.

The 50 μm core size fibre cables experienced similar power loss, each coupling average normalized power values between 0.41 and 0.42. In contrast, the OM1 fibre cable demonstrated the highest power coupling under lateral misalignment, achieving an average normalized power of 0.62. It's worth noting that the average normalized power coupled into the multi-mode fibre cables corresponds to the ratio of the fibre core sizes and the tested range. However, the average normalized power coupled into the single-mode fibre does not align with this ratio due to the greater focal spot size compared to the fibre core.

Angular misalignment was introduced at the tips of the fibre cables, as detailed in Sec. 4.1.1.2. The beam underwent a total tilt of 300 mrad, ranging from -150 mrad to 150 mrad. It's important to note that the angular offset depicted in Fig. 4.8(a) exceeds the encoded limit of 150 mrad on the positive x-axis, primarily due to the initial angular error. Furthermore, the range of angles tested was constrained by the size of the SLM screen and the focal length of the receiving lens. Despite these limitations, the impact of angular misalignment on coupled power remains evident. As illustrated in Fig. 4.8(a), all fibre cables experienced reduction in coupled power under angular misalignment.

With a numerical aperture of 0.14, the single-mode fibre demonstrated the least resilience to focal point tilt, coupling the lowest average normalized power of 0.41, as illustrated in Fig. 4.8(b). In contrast, the multi-mode fibre cables, featuring a numerical aperture of 0.2 (OM2 to OM5), exhibited higher power coupling under angular misalignment, with an average normalized power ranging between 0.57 and 0.58. Notably, the OM1 fibre cable, with a numerical aperture of 0.27, achieved the highest power coupling under this misalignment, recording an average normalized power of 0.62. These results emphasise that a greater numerical aperture enhances the resilience of fibre cables, enabling them to couple more light under angular misalignment.

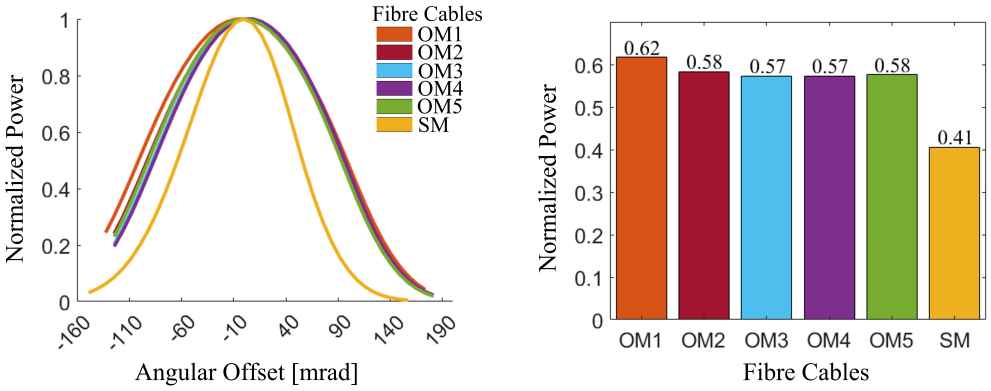
The impact of longitudinal misalignment on fibre coupling was observed by manipulating the position of the beam focal spot along the fibre axis (z-axis). This manipulation



(a) Lateral misalignment

(b) Average coupled power under lateral misalignment

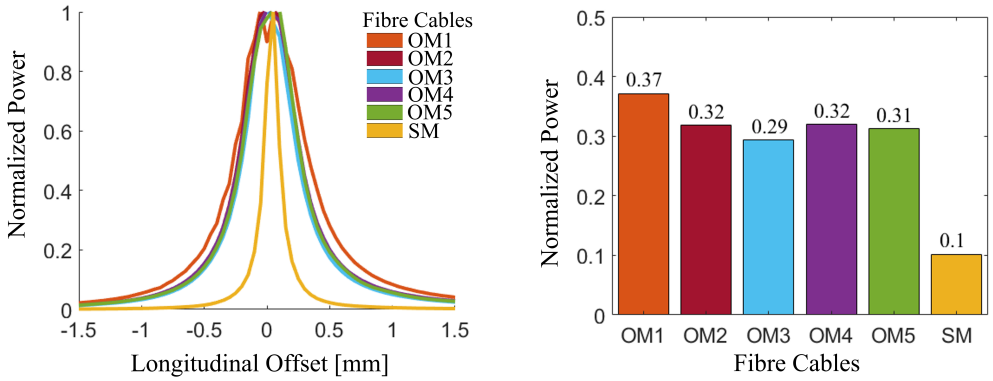
Figure 4.7: The impact of focal point lateral misalignment on coupling into standard fibre cables. The lateral shift ranges from -60 μm to 60 μm. Notably, the OM1 fibre cable demonstrates the highest average normalized power, whereas the single-mode fibre exhibits the least coupling under this misalignment condition.



(a) Angular misalignment

(b) Average coupled power under tilt misalignment

Figure 4.8: The impact of focal point angular misalignment on coupling into standard fibre cables. As the angular offset increases, a decrease in coupled power is observed across all fibre cables. Among them, the OM1 fibre cable exhibits the highest average normalized power, while the single-mode fibre demonstrates the lowest under this misalignment.



(a) Longitudinal misalignment

(b) Average coupled power under longitudinal misalignment

Figure 4.9: Impact of longitudinal misalignment on coupling into standard fibre cables. The longitudinal offset varies within the range of -1.5mm to 1.5mm. Among the fibres, the OM1 fibre cable exhibited the highest average normalized power, while the single-mode fibre showcased the lowest.

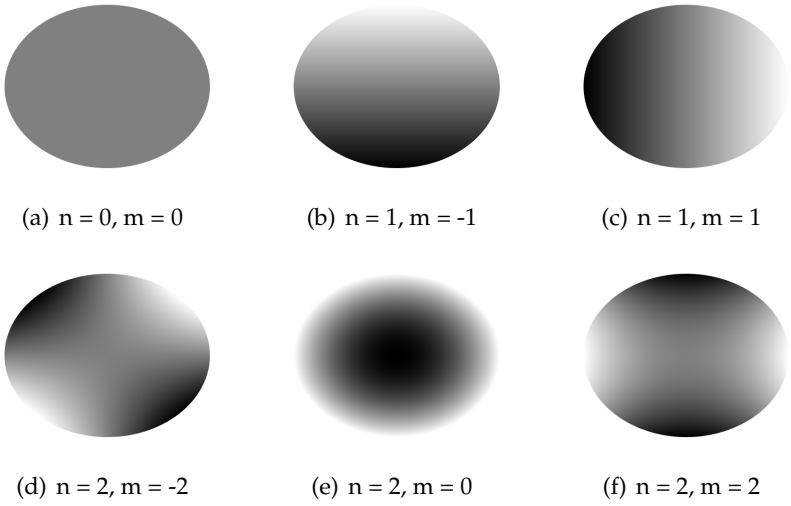
essentially involved defocusing the incident light on the fibre tip, affecting both the focal spot size and numerical aperture of the incoming beam. A total longitudinal offset range of 3 mm (-1.5 mm to 1.5 mm) was applied to the fibre cables. As depicted in Fig 4.9(a), all fibres experienced power loss within this range.

Among the fibres, the OM1 fibre cable demonstrated the highest resilience to longitudinal misalignment, coupling an average normalized power of 0.37 across this range, as illustrated in Fig 4.9(b). The OM2, OM4, and OM5 multi-mode fibre cables exhibited similar coupling losses, with average normalized power values ranging between 0.31 and 0.32. The OM3 fibre cable recorded the lowest average optical power among the multi-mode fibre cables, with an average normalized power of 0.29. In contrast, the single-mode fibre cable proved to be the least resilient to longitudinal misalignment, as indicated by its narrow curve in Fig 4.9(a), and only coupling an average normalized power of 0.1.

The results demonstrate a clear correspondence between the power coupled into the fibre cable under misalignment and their physical attributes. As expected, larger fibres maintain higher coupled power under various misalignment conditions. The OM1 fibre cable, characterised by the largest fibre core size and widest numerical aperture, consistently demonstrated the highest power coupling across all misalignment tests. The 50 μm core fibre cables exhibited similar performance under lateral and angular misalignment. However, during longitudinal misalignment, the OM3 fibre cable displayed lower coupled power compared to the other multi-mode fibres, emphasising its greater sensitivity to this specific misalignment condition. The single-mode fibre exhibited the least favourable coupling performance under all forms of misalignment.

4.2 Fibre coupling in atmospheric turbulence

The adverse effects of atmospheric turbulence on propagating light signals, detailed in Chapter 2.4, hinder fibre coupling, leading to subsequent power loss. To assess the impact of turbulence on coupling into standard fibre cables, we measured the power coupled into them under systematically induced turbulence. Simulating turbulence becomes crucial as real-world turbulence is inherently random and dynamic. This controlled and repeatable



(a) n = 0, m = 0 (b) n = 1, m = -1 (c) n = 1, m = 1

(d) n = 2, m = -2 (e) n = 2, m = 0 (f) n = 2, m = 2

Figure 4.10: Examples of generated Zernike polynomials which represent the following aberrations: piston (a), vertical tilt (b), horizontal tilt (c), oblique astigmatism (d), defocus (e) and vertical astigmatism (f).

testing approach allows for a comprehensive evaluation of the fibre cables' performance under turbulent conditions

Simulating atmospheric propagation involves encoding turbulent phase screens on optical devices such as an SLM. These phase screens represent individual instances of atmospheric phase perturbations, generated by transforming random computer-generated numbers into a grid of phase values that mimic the statistical properties of turbulence-induced phase fluctuations. The optical phase used for generating these screens can be expressed as a weighted sum of basis functions. Common basis sets include Zernike's polynomials and Fourier series. Notably, the Fourier series method may lack accuracy in producing phase screens due to its inability to sample spatial frequencies at a sufficiently low resolution, particularly for representing low-order modes like tilt [78]. Zernike polynomials overcome this limitation, ensuring more accurate representation.

4.2.1 Simulation of atmospheric turbulence using Zernike polynomials

Zernike's polynomials form a set of orthogonal mathematical expressions which describe phase aberrations within circular wavefronts as illustrated in Fig. fig:Zernikes [79]. The orthogonality of Zernike polynomials allows for a wavefront to be described as their linear sum, with each polynomial having a specific weighting coefficient. Such a wavefront can be expressed in polar coordinates (with a radius r and angle θ) as

$$\phi(r,\theta) = \sum_{n=-\infty}^{\infty} \sum_{m=-\infty}^{n} C_n^m Z_n^m(r,\theta), \tag{4.10}$$

where C_n^m represents the weighting coefficients of the Zernike polynomials denoted by Z_n^m [80]. The Zernike polynomials are expressed as

$$Z_n^m(r,\theta) = \begin{cases} R_n^m(r)\cos(m\theta), & \text{for } m \geq 0 \\ R_n^m(r)\sin(m\theta), & \text{for } m < 0 \end{cases}. \tag{4.11}$$

This expression is only valid when the indices m and n satisfy $m \leq n$ and $n - |m| =$ even. Here, r should be confined within a unit circle ($0 \leq r \leq 1$), and θ is measured clockwise

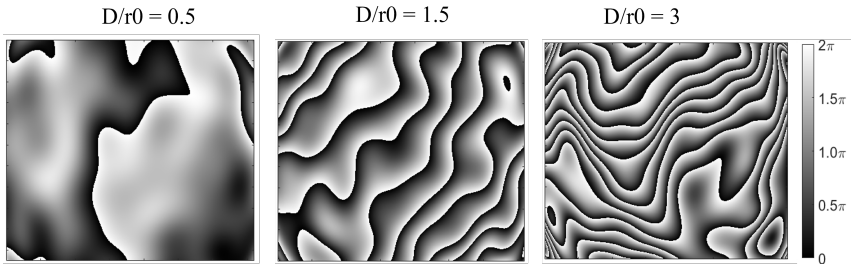


Figure 4.11: Turbulent phase screens generated at different turbulence strengths. The phase spans from 0 to 2π.

from the positive y-axis. The radial function R_n^m is expressed as

$$R_n^m = \sum_{l=0}^{(n-m)/2} \frac{(-1)^l (n-l)!}{l! \left[\frac{1}{2}(n+m)-l\right]! \left[\frac{1}{2}(n-m)-l\right]!} r^{n-2l}. \tag{4.12}$$

The Zernike polynomials are encoded to overfill the SLM, whose dimensions are 14.4mm by 10.5mm. This results in a circle surrounding the SLM screen with a radius of 8.91mm. The radius of the generated Zernike polynomials, denoted as r, is normalized by the physical radius of 8.91 mm to satisfy the requirement for a unity radius. The Noll matrix is used to assign appropriate weighting coefficients (C_n^m) which align with the statistical properties of Kolmogorov turbulence. The Noll matrix, denoted by I_{nm}, is generated by computing the spatial covariance matrix derived from the Zernike expansion which gives

$$I_{nm} = \frac{0.15337(-1)^{n-m}(n+1)\Gamma(14/3)\Gamma(n-5/6)}{\Gamma(17/6)^2\Gamma(n+23/6)}. \tag{4.13}$$

Assuming that the weighting coefficients follow a normal distribution with a mean of zero, their variance is calculated from the Noll matrix as

$$\sigma_{nm}^2 = I_{nm}\left(\frac{D}{r_0}\right)^{5/3}, \tag{4.14}$$

where D denotes the aperture diameter and r_0 signifies the Fried parameter. D/r_0 signifies the strength of atmospheric turbulence. Weighting coefficients (C_n^m) of specific turbulence strengths are generated by random drawings from a normal distribution with zero mean and standard deviation of σ_{nm} [81]. The weighting coefficients are multiplied by their corresponding Zernike polynomials, which are then summed to generate turbulent phase screens, as shown in Eq. 4.10. 250 weighted Zernike polynomials are used to generate random phase screens of specific turbulence strengths, as illustrated in Fig4.11.

4.2.2 Experimental set-up and calibration of turbulence phase screens

The experimental setup shown in Fig. 4.12, was used to measure the optical power coupled into the fibre cables under atmospheric turbulence. This setup was a modified version of the experimental setup used to induce misalignment, shown in Fig. 4.2. A 1550 nm Gaussian beam was emitted from a single-mode fibre cable and collimated at 3.42 mm. The beam was directed to the SLM, on which turbulent phase screens were encoded with a diffraction grating. Lenses L1 and L2, each with a focal length of 150 mm, were used as a 4f telescope to relay the Gaussian beam onto the SLM while avoiding beam divergence. The beam emerging from the SLM underwent spatial filtering to only permit the first diffraction order. This was performed using a pinhole aperture and lens L3. Lens L4 collimated the beam,

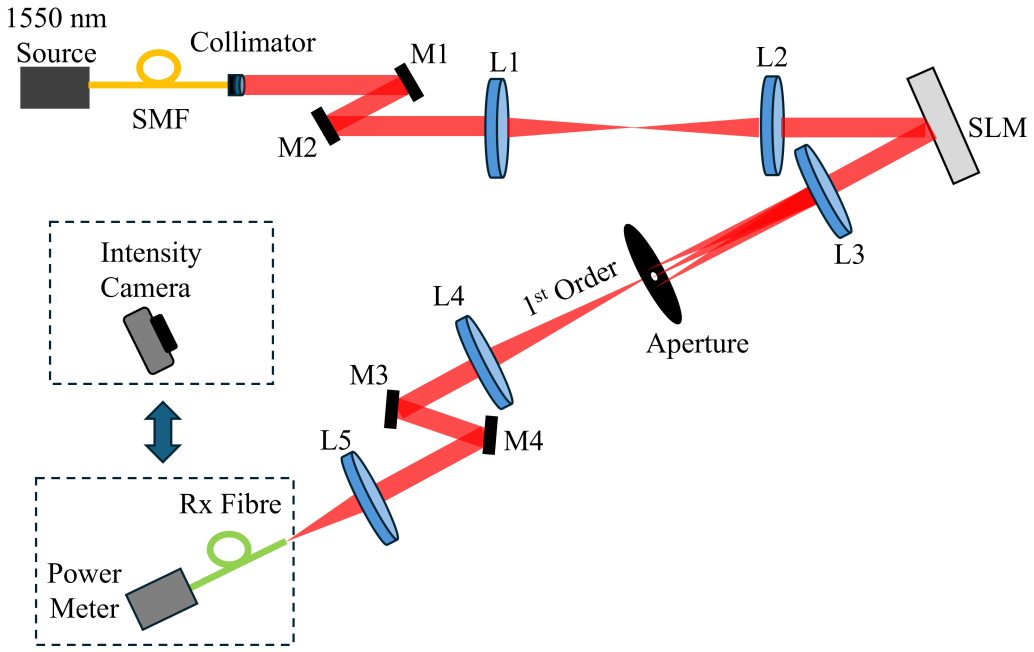


Figure 4.12: Experimental setup to observe the effects of simulated turbulence on the power coupled into the standard fibre cables. SMF represents a single mode fibre while Rx Fibre represents the different fibre cables tested. M1, M2, M3 and M4 represent mirrors used for alignment. Lenses L1 and L2, each with a focal length of 150 mm, relay the beam from the collimator to the SLM. Lenses L3 and L4 each have a focal length of 200 mm. Lens L5, with a focal length of 30 mm, focuses the beam onto the fibre cables.The intensity camera replaces the receiving fibre (Rx Fibre) and the power meter during the calibration of turbulence strength.

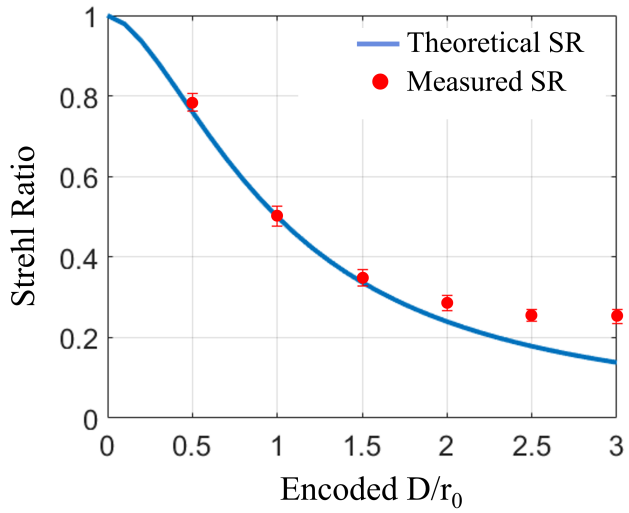


Figure 4.13: Verification plot of the measured Strehl ratio (Strehl Ratio (SR)) against theoretical Strehl ratio. 200 measurements were made for each value of D/r_0. The errorbar represent standard error.

which was directed to the receiving fibre (labelled as Rx Fibre) using mirrors M3 and M4. Lens L5, with a focal length of 30 mm, was used to focus the beam onto the fibre cable.

Before conducting the tests, the turbulence strength of the phase screen had to be calibrated to match the theoretical turbulence strength at given values of D/r_0. This involved an iterative process of manipulating the D/r_0 ratio and measuring the resulting Strehl ratio. The Strehl ratio was measured by replacing the receiving fibre cable and power meter in Fig. 4.12 with an infrared intensity camera. To calculate the Strehl ratio, the average central intensity of the beam under a specific turbulence strength was divided by its central intensity in the absence of turbulence. The average central intensity for each turbulence strength was calculated using 200 randomly generated phase screens. The measured Strehl ratio values were compared to the theoretical Strehl ratio for the given D/r_0 values.

While the turbulent phase screens were encoded at an aperture diameter of 17.82 mm to overfill the SLM, the collimated beam diameter emerging from the single-mode fibre was approximately 3.42 mm. Due to this discrepancy, the turbulence strength appeared weaker than what was encoded. To mitigate this, the value of D/r_0 was multiplied by a factor of 5.21 (phase screen diameter / collimated beam diameter). Additionally, the D/r_0 value was further multiplied by a factor of $\sqrt{2}$, representing the approximated ratio of the effective telescope diameter to the Gaussian beam diameter [56]. The generated turbulence strength was verified by comparing the measured Strehl ratio to the theoretical Strehl ratio given by Eq. 2.28 at different D/r_0 values. This verification is shown in Fig. 4.13.

4.2.3 Effect of simulated turbulence on coupled power

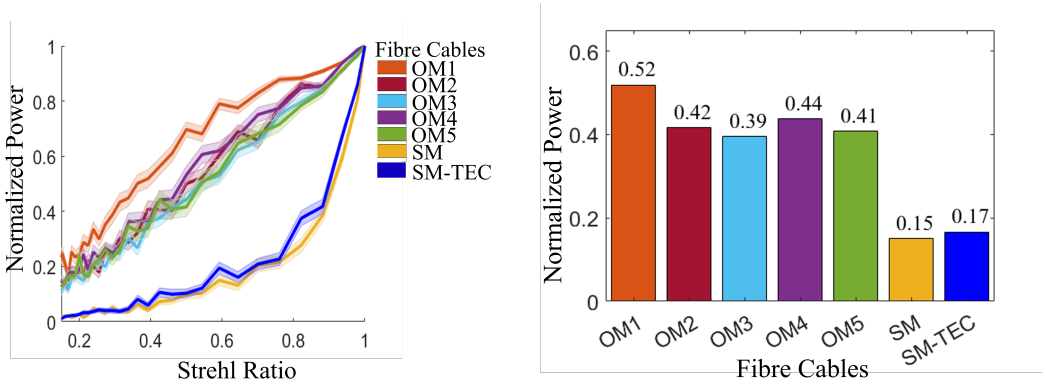
Atmospheric turbulence causes amplitude and phase distortions in propagating light signals, negatively affecting fibre coupling. Consequently, lower optical power is expected to be coupled into the receiving fibre cables in stronger turbulence conditions. This pattern is evident in Fig 4.14(a), where an increase in the normalized power coupled into the standard fibre cables is observed as the Strehl ratio increases, indicating weaker turbulence.

The single-mode fibre cable exhibited the lowest coupled power in this experiment, particularly for Strehl ratio values below 0.8. This can be attributed to its small core size and numerical aperture. Furthermore, while turbulence-induced phase distortion shifts power from the Gaussian mode to high-order modes [82, 83], the single-mode fibre is designed to exclusively support Gaussian beams. The power coupled into the high-order modes is thus lost when coupling into a single-mode fibre.

A Thermally-Expanded Core Single mode fibre (SM-TEC) cable was introduced to the experiment and compared to the standard single-mode fibre cable. This fibre cable has a core size of 19 μm and Numerical Aperture (NA) of 0.06. Despite having a thermally-expanded core, the SM-TEC fibre exhibited similar performance to standard single-mode fibre, with average normalized power values of 0.17 and 0.15, as shown in Fig 4.14(b), respectively. This similarity arises because both single-mode fibres only support the Gaussian mode.

The multi-mode fibre cable exhibited enhanced power coupling under simulated turbulence. Similarly, the 50 μm core fibre cable demonstrated consistent performance, with average normalized power values ranging from 0.39 to 0.44. This comparative performance is visually depicted in Fig. 4.14(a), where the power coupled into these fibres overlaps across various turbulence strengths. The OM1 fibre cable demonstrated the highest average normalized power, reaching 0.52. This is attributed to its larger core size and numerical aperture which allow it to capture more light. Furthermore, the fibre also supports the highest number of modes, making it more resilient in coupling higher-order modes from free-space.

The vertical and horizontal tilt aberrations remain the largest contributors to turbulence-induced distortion, with 87% of the phase variance attributed to them [84, 85]. Amongst the effects of these aberrations are lateral and angular misalignment, which have been shown in Sec. 4.1 to severely affect the power coupled into the fibre cables. To assess the impact of higher-order modes, Zernike polynomials associated with vertical and horizontal tilt



(a) Coupled power under simulated turbulence

(b) Average coupled power under all turbulence strengths

Figure 4.14: Effect of simulated turbulence on fibre coupling. The average power coupled at specific turbulence strengths is calculated across 100 measurements. The shaded region represents the standard error (a). Additionally, an average of the power coupled into each fibre cable across all turbulence strengths is presented (b). The OM1 fibre cable records the highest coupled power in the presence of simulated turbulence.

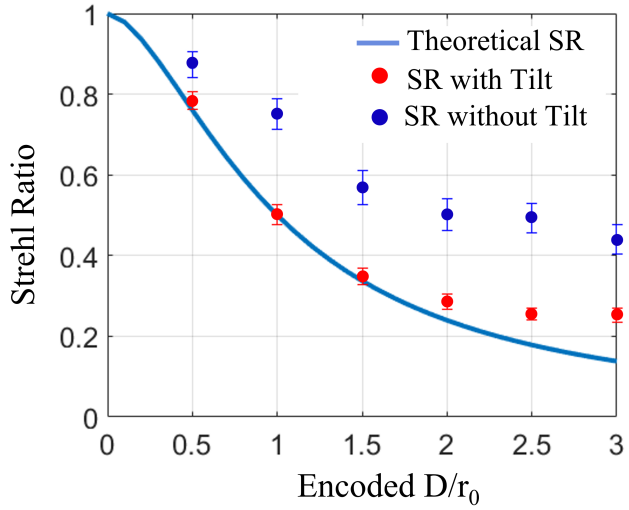
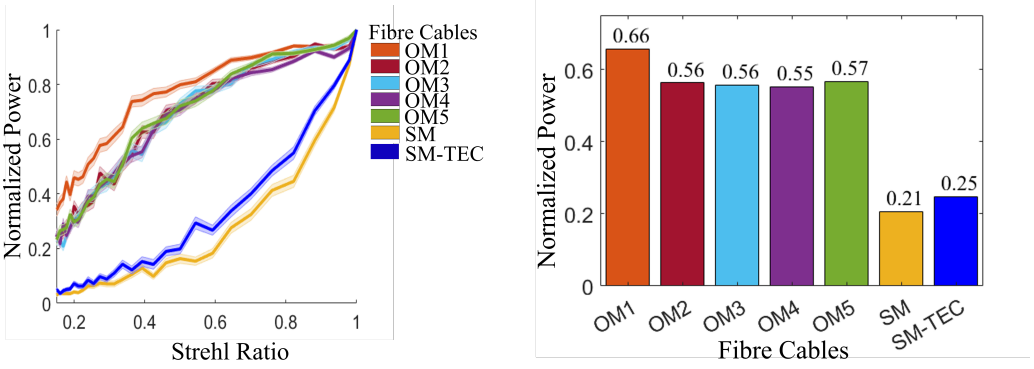


Figure 4.15: Verification plot of the measured Strehl ratio (SR) against theoretical Strehl ratio. The blue dots indicate the measured Strehl ratio in the absence of tilt aberrations. Excluding tilt results in weaker turbulence strength.

aberrations (n = 1, m = 1 and n = 1, m = -1) were intentionally excluded from the phase screen generation process. The omission of the tilt aberrations resulted in phase screens characterised by a weaker turbulence strength. Tilt aberrations contribute a significant part to the effects of atmospheric turbulence on propagating light signals. For this reason, SR measurements with tilt provide a more accurate representation of turbulence than those without tilt, thus fitting the turbulence model better, as illustrated in the verification plot presented in Fig. 4.15.

The impact of higher-order modes is illustrated in Fig. 4.16, where all fibre cables exhibit higher power coupling in the absence of tilt aberrations. Without tilt, the dominance of



(a) Coupled power under simulated turbulence

(b) Average coupled power under all turbulence strengths

Figure 4.16: The effect of higher-order aberrations on fibre coupling. The phase screens generated excluded the low-order tilt aberrations. Average power coupled at specific turbulence strength is calculated across 100 measurements, with the shaded region representing the standard error (a). An average of the power coupled into each fibre cable across all turbulence strengths is presented (b). The OM1 fibre cable records the highest coupled power in the presence of higher-order modes.

second-order Zernike aberrations (defocus and astigmatism) is evident [79]. Under these conditions, the thermally expanded core of the SM-TEC fibre allows it to couple slightly more light than the standard single-mode fibre, attributed to its larger core size. Fibres with larger core sizes couple more power when faced with defocus, as seen in the longitudinal misalignment results depicted in Fig. 4.9. The SM-TEC achieves an average normalized power of 0.25, while the standard single-mode fibre records an average normalized power of 0.21. These results indicate that even in the absence of tilt, phase distortions caused by higher-order aberrations hinder coupling into single-mode fibres.

In contrast, coupling into the multi-mode fibres significantly improved in the absence of tilt aberrations. The 50 μm multi-mode fibres demonstrated consistent performance, with an average normalized power ranging between 0.55 and 0.57, as depicted in Fig. 4.16(b). This indicates that higher-order modes affect coupling into multi-mode fibres of equal dimensions in a similar manner. The OM1 fibre cable showcased the highest power coupling in this experiment, with an average normalized power of 0.66, surpassing the average normalized power of 0.52 it coupled in the presence of tilt. This superior performance is again attributed to the fibre's larger dimensions and its ability to support a greater degree of higher-order modes.

4.3 Conclusion

Fibre coupling is integral to successful FSO communication. However, the stringent alignment requirements make it sensitive to non-ideal conditions. This chapter characterised the coupling performance of standard fibre cables under focal point misalignment and simulated turbulence. Focal point misalignment explored lateral, angular, and longitudinal misalignment. These forms of misalignment were induced by manipulating the grating frequency and hologram position encoded on an SLM. A Fourier lens was encoded onto the SLM to induce longitudinal misalignment. Under these misalignment conditions, the OM1 fibre cable consistently outperformed the other fibre cables, by coupling the highest amount of normalized power. This is due to its larger core size and wider numerical aperture. In

contrast, having the smallest dimensions, the single-mode fibre cable coupled the lowest optical power under all forms of misalignment. The fibre cables of 50 μm core size and NA of 0.2 (OM2-OM5), showcased comparable results under misalignment. These results highlighted the relationship between the fibre cable dimensions and their resilience to coupling light under misalignment.

Atmospheric turbulence was simulated by generating turbulent phase screens using a sum of weighted Zernike polynomials. The turbulence strength was varied while the power coupled into the fibre cables was measured. The OM1 fibre cable proved to be most resilient to the effects of simulated turbulence by coupling the highest amount of power across the different turbulence strengths. The other multi-mode fibre cables had comparable performances, with the OM4 fibre having the highest average power while the OM3 the lowest amongst them. The worst coupling performance under turbulence was experienced by the single-mode fibre cable. The effects of higher-order aberrations were observed by excluding the tilt aberrations. This resulted in weaker generated turbulence, allowing all fibre cables to experience greater fibre coupling under these conditions. The OM1 fibre cable coupled the highest normalized power, while the other multi-mode fibre cables coupled approximately equal normalized power, suggesting similar performance under higher-order aberrations. The single-mode fibre was the least tolerant to the higher-order aberrations, showcasing the lowest coupled power. The results of the turbulence tests showed the ability of fibre cables which support a greater degree of higher-order modes to couple more phase-distorted light.

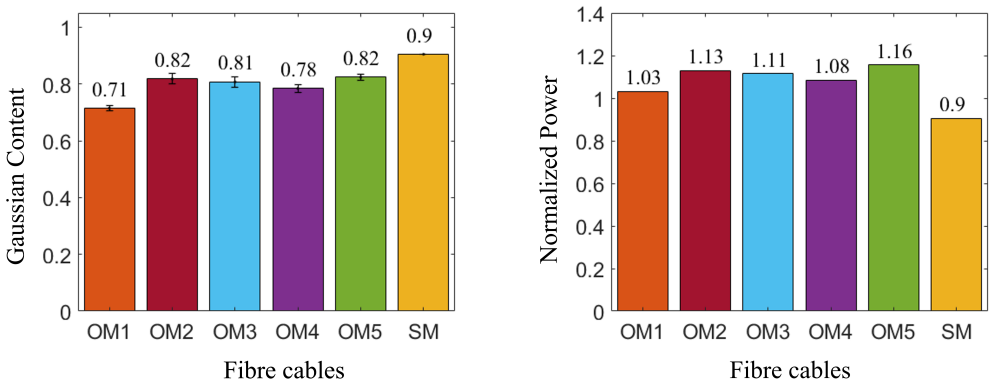
CHAPTER 5

Integrated Analysis of Transmitter and Receiver Performance

The integration of low-cost telecommunication fibre cables in Free Space Optical (FSO) systems offers a promising opportunity to reduce the overall cost and complexity of FSO technology, making it more accessible and easier to deploy. As discussed in the preceding chapters, we have characterised the transmission and reception performances of these fibre cables for free-space applications. The transmitter characterisation in Chapter 3 focused on analysing the power launched out of the fibre cables in the fundamental Gaussian mode. Meanwhile, the receiver characterisation in Chapter 4 delved into assessing the power coupled from free-space to the fibre cables under non-ideal conditions, including misalignment and simulated atmospheric turbulence. This chapter serves to consolidate these separate characterisations by examining the received power in atmospheric turbulence when different combinations of fibre cables are used for transmission and reception.

Small Form-factor Pluggable (SFP) transceiver-based FSO systems can be designed using standard or bidirectional SFP transceiver modules, as discussed in Chapter 1. When utilising standard transceivers, two separate fibre cables are employed to transmit and receive optical signals. This setup establishes two unidirectional FSO channels, each transmitting signals from a transmit fibre to a receive fibre. On the other hand, bidirectional SFP transceivers enable the use of one fibre cable for both transmission and reception at each end of the link. Previous SFP-based FSO systems have utilised single-mode to multi-mode transmission with standard SFP transceivers [42], and single-mode to single-mode transmission when using bidirectional SFP transceivers [36]. In this chapter, we investigate the received power when employing various combinations of telecommunication fibre cables for both unidirectional and bidirectional transmission.

The transmitter characterisation, in Chapter 3, revealed that SFP A exhibited better quality than SFP B, as evidenced by higher Gaussian content and fewer fluctuations in the transmitted power. Therefore, the transmission results obtained from SFP A will be utilised in this analysis. The transmitted Gaussian content and normalised Gaussian power are presented again in Fig. 5.1. A summary of the average normalised power coupled into each fibre cable across different turbulence strengths is provided in Fig. 5.2.



(a) Gaussian Content

(b) Normalized Gaussian power

Figure 5.1: Gaussian content in optical fields launched from the fibre cables (a). The product of the Gaussian content and the total power transmitted by the fibre cable relative the the total power transmitted by the single-mode fibre cable.

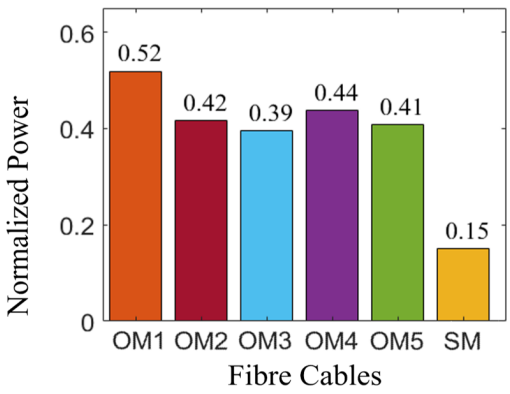


Figure 5.2: Average normalized power coupled into the fibre cables in the presence of simulated turbulence. The average power is calculated across all generated turbulence strengths.

5.1 Unidirectional transmission

Fig. 5.3 demonstrates the setup of a unidirectional link using two distinct fibre cables for transmission and reception. This approach allows for the selection of the most suitable fibres for both transmitting and receiving, which is particularly beneficial in SFP-based FSO systems employing standard SFP modules.

When considering equal optical power transmission through the fibre cables, the Gaussian content shown in Fig. 5.1(a) represents the amount of power each fibre transmits in the Gaussian mode. We assume that the majority of power in the Gaussian mode is effectively captured within the receiving aperture, while higher-order modes extend beyond the aperture's size. By multiplying this transmitted Gaussian power by the average power coupled under simulated turbulence, we obtain the received Gaussian power under turbulence, as shown in Fig. 5.4.

In these conditions, the highest received power is observed when the single-mode fibre is utilised as the transmitter and the OM1 fibre cable as the receiver. This outcome is expected as the single-mode fibre transmits the highest Gaussian content, while the OM1 fibre cable, having the largest dimensions, demonstrates superior power coupling under

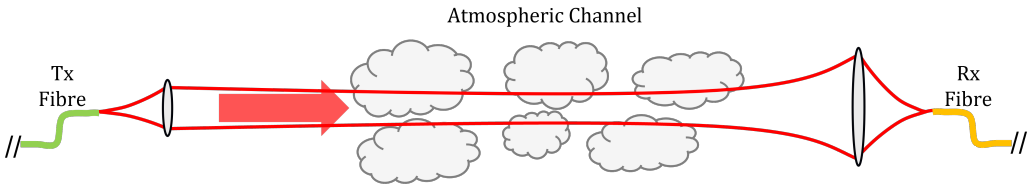


Figure 5.3: Unidirectional transmission of a light beam from a transmit fibre to a receive fibre across a turbulent atmospheric channel.

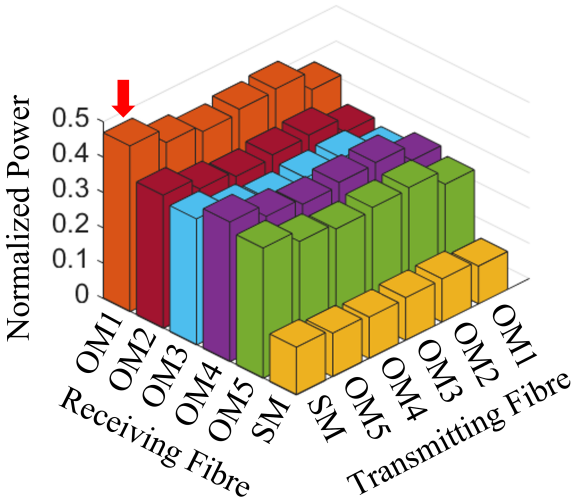


Figure 5.4: Average received Gaussian power in the presence of atmospheric turbulence. This is calculated by multiplying the Gaussian content transmitted by the fibre cables, by the average power coupled into the fibre cables under simulated turbulence. The arrow points to the highest received power.

atmospheric turbulence. Conversely, the poorest performance is observed when using the OM1 fibre cable for transmission and the single-mode fibre for the reception. This is primarily attributed to the single-mode fibre's inadequate coupling performance under atmospheric turbulence, compounded by the OM1 fibre cable's transmission of the lowest Gaussian content.

Moreover, in an SFP-based FSO system, the optical power transmitted through the different fibre cables varies depending on the cable's size, with larger fibre cables transmitting higher optical power than smaller ones. This discrepancy results in greater Gaussian power in the multi-mode fibre cables, as depicted in Fig. 5.1(b). Here, the Gaussian power is the product of the Gaussian content and the total power emitted by the fibre cables relative to that transmitted by the single-mode fibre.

When this transmitted Gaussian power is multiplied by the average power coupled in turbulence, the resulting received Gaussian power is shown in Fig. 5.5. In this analysis, the highest received power is observed when the OM5 fibre is used as the transmitter and the OM1 fibre as the receiver. This outcome can be attributed to the OM5 fibre's capability to efficiently channel high power from the SFP module and maintain it in the Gaussian mode. As anticipated, the OM1 fibre cable proves to be the most effective receiver. Furthermore, despite the single-mode fibre exhibiting the highest Gaussian content, it transmits the lowest amount of power from an SFP module and couples the least amount of power under atmospheric turbulence, as depicted in Fig. 5.2. Consequently, the transmission from

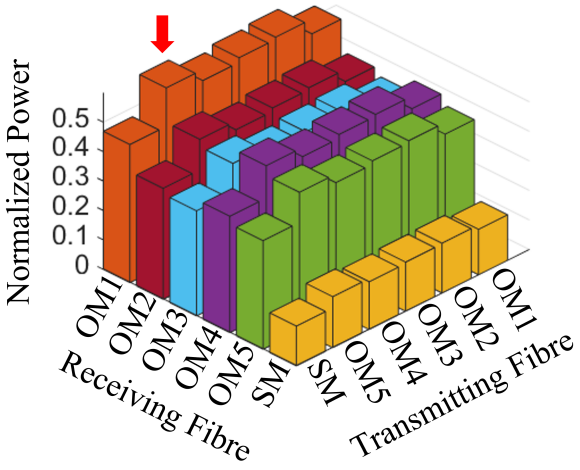


Figure 5.5: Average received Gaussian power in the presence of atmospheric turbulence, relative to the total power transmitted by the single-mode fibre. This is calculated by multiplying the Gaussian power relative to the total power transmitted by the single-mode power, by the average power coupled into the fibre cables under simulated turbulence. The arrow points to the highest received power.

single-mode fibre to single-mode fibre yields the lowest received optical power.

5.2 Bidirectional transmission

The opportunity to use few components in an SFP-based FSO system arises when bidirectional SFP transceivers are used. In such a system, the same fibre cable is used on both sides of the link as depicted in Fig 5.6. Employing a fibre cable which excels in both roles would be beneficial for such a system.

Again,we examine scenarios where equal power is transmitted through the fibre cables, as well as practical cases of transmission from an SFP transceiver, where the power transmitted through the different fibre cables varies. In the case of equal power transmission, the received Gaussian power is calculated by multiplying the Gaussian content transmitted through each fibre by the average power coupled into the same fibre in the presence of atmospheric turbulence, as depicted in Fig. 5.7(a). Conversely, for scenarios where power transmission varies, the received Gaussian power is calculated by multiplying the transmitted Gaussian power in each fibre relative to the single-mode by the average power coupled into the same fibre in the presence of atmospheric turbulence, as shown in Fig. 5.7(b).

The results exhibit a consistent trend, with the OM1 fibre cable receiving the highest power, while the other multi-mode fibres demonstrating similar performances as illustrated in Fig. 5.7. Conversely, the single-mode fibre receives the lowest optical power. The superior performance of the OM1 fibre cable over the others in this assessment can be attributed to its significantly better coupling performance in the presence of atmospheric turbulence. Additionally, although the OM2, OM4, and OM5 fibres exhibit slightly different transmission and coupling performances, they demonstrate comparable results in this assessment. It's worth noting that while comparable, the OM3 fibre cable receives the lowest power among the multi-mode fibres in this bidirectional assessment. These findings underscore the critical role of coupling performance in the overall effectiveness of a bidirectional FSO system.

While the results discussed above show the bidirectional performance of the fibre cables

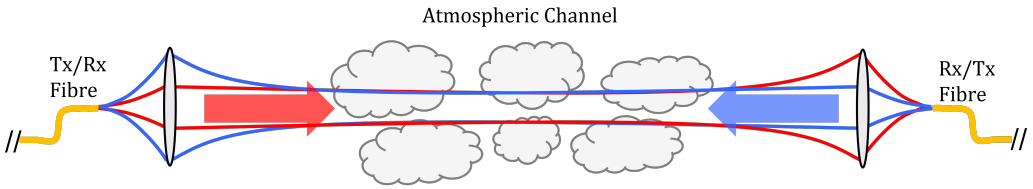
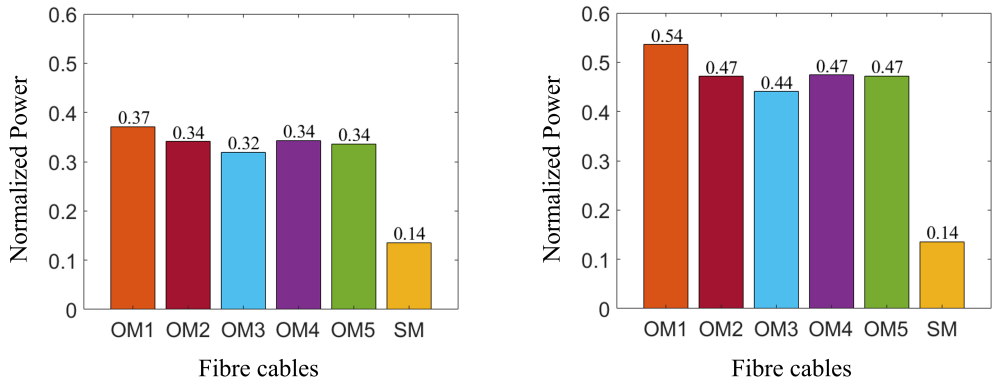


Figure 5.6: Bidirectional transmission of two optical signals with different wavelengths across a turbulent atmospheric channel. Each fibre cable serves as both a transmitter and receiver.



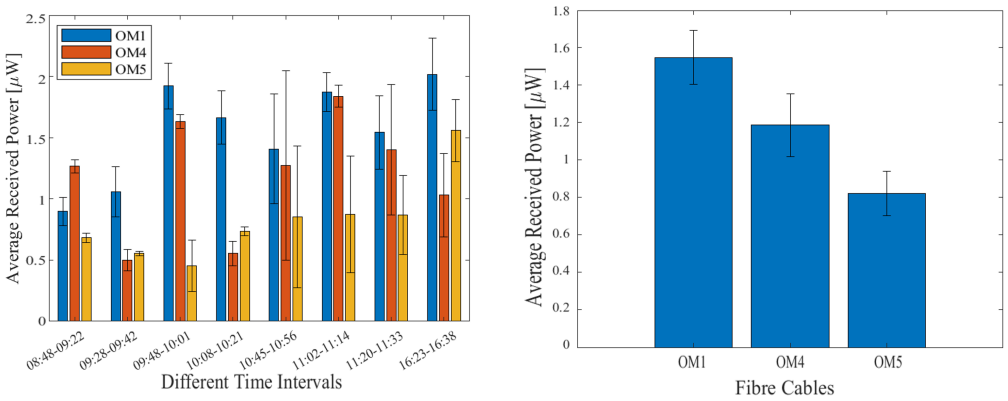
(a) Received Gaussian Power when equal power is transmitted through the fibre cables

(b) Received Gaussian Power relative to the single-mode fibre.

Figure 5.7: Received Gaussian power transmitted in a bidirectional arrangement, in the case of equal transmitted power (a) and power normalized to the power transmitted by the single-mode fibre.



Figure 5.8: Experimental bidirectional FSO system. The system utilises a plano-convex lens with a diameter of 75 mm and focal length of 200 mm.



(a) Received power across different time

(b) Average received power

Figure 5.9: Average received power measured in a real-world bidirectional FSO system. Average received power across different times of the day (a). Average received power in each fibre cable across all time intervals measured.

in the presence of simulated turbulence, other effects of the atmosphere are negated. As such we test the fibre cables in real-world conditions using an experimental bidirectional FSO system shown in Fig. 5.8. This system comprised a single plano-convex lens on each side of the link, with a diameter of 75 mm and focal length of 200 mm. With these lens parameters, the calculated numerical aperture and focal spot size are 0.18 and 8.27 μm respectively.

The OM1, OM4 and OM5 multi-mode fibre cables were tested using this system across a propagation length of 383 m between two buildings at the University of the Witwatersrand. A 1510/1590 nm bidirectional SFP module was used as the light source on one building, an infrared power meter operating at a sampling time of 120 ms was used to measure the received power on the other building. The fibre cables were tested in a bidirectional configuration, where the same type of fibre was used to transmit and receive. A total of eight data sets were collected for each fibre cable across different times of the day. Each data set was recorded for 3 minutes.

The average received power across various time intervals is presented in Fig. 5.9(a), with an overview of these averages depicted in Fig. 5.9(b). In these analyses, the OM1 fibre cable consistently demonstrates the highest received power, followed by the OM4 fibre and subsequently the OM5 fibre cable. This observed superiority of the OM1 fibre aligns with its bidirectional performance showcased in Fig. 5.7. However, while the performances of the OM4 and OM5 fibre cables appear comparable in Fig. 5.5, the real-world assessment reveals that the OM4 fibre records a higher average received power, as illustrated in Fig. 5.9(b). This discrepancy could potentially indicate instances of stronger turbulence during the measurements, favouring the performance of the OM4 fibre, as suggested by its greater resilience to atmospheric turbulence, as demonstrated in Fig. 5.2.

5.3 Conclusion

The successful operation of a fibre-based FSO system relies on both the transmission and reception performances of the fibre cables used. This chapter evaluated the performance of various combinations of transmitting and receiving fibre cables by examining both the Gaussian power transmitted and the received power under turbulence conditions.

In scenarios where equal power is transmitted through all fibre cables, the combination of a single-mode fibre transmitting to an OM1 fibre resulted in the best performance. This was because the single-mode fibre transmitted the highest Gaussian content, while the OM1

coupled the highest amount of power in the presence of atmospheric turbulence. Conversely, the combination of transmitting from an OM1 fibre and receiving with a single-mode fibre exhibited the poorest performance.

When transmitting from an SFP transceiver, multi-mode fibre transmits more power than single-mode fibre, resulting in higher Gaussian power. Thus, the combination of transmitting from the OM5 and receiving into the OM1 fibre cables yielded the best performance. Conversely, the worst performance was observed when a single-mode fibre transmitted to another single-mode fibre. This was attributed to the single-mode fibre's lower power transmission from the SFP and its reduced power coupling in the presence of turbulence.

In the bidirectional configuration, where one type of fibre cable is used for both transmission and reception, a similar pattern is observed between equal power transmission and transmission from an SFP transceiver. The OM1 fibre cable consistently outperformed the other fibre cables in both scenarios, owing to its superior coupling ability, which enables it to capture more light effectively. The performance of the other multi-mode fibres was comparable, with the OM3 fibre exhibiting the lowest received power among them. Given the significant reliance on the receiver's capacity, it has been demonstrated that the OM1 fibre cable is the best-performing fibre cable in a bidirectional FSO system. This conclusion is further supported by experimental FSO link results, where the OM1 fibre cable received more power compared to the OM4 and OM5 fibre cables.

CHAPTER 6

Summary

FSO communication could significantly benefit communities residing outside traditional fibre coverage networks by providing them with fast and dependable internet connectivity. However, commercial FSO systems are often expensive and inaccessible to such communities. Utilising low-cost telecommunication hardware in FSO systems could potentially improve their cost-effectiveness. SFP transceiver modules have received attention for this purpose due to their high-power lasers and sensitive photodiodes. SFP transceiver-based FSO systems commonly employ short fibre cables to transmit and receive optical signals across the atmosphere. Despite the critical role of fibre cables in such systems, it remained unclear which type(s) would be most suitable for transmission and reception. Particularly in challenging conditions such as misalignment and atmospheric turbulence.

The purpose of this research was to investigate the transmission and reception performances of standard telecommunication fibre cables, in particular those defined in the ISO/IEC 11801 international standard. These fibre cables are the standard single-mode fibre and five classes of multi-mode fibre (OM1-OM5). The central research question which guided this work was, *How do different telecommunication fibre cables compare in terms of transmit performance and free-space coupling performance?* Characterisations of transmission and reception performances were presented separately in Chapters 3 and 4, respectively. In Chapter 5, we consolidated these separate characterisations by analysing the performance of different transmitting and receiving fibre cable combinations.

Preceding these chapters, Chapter 2 provided background information on factors affecting SFP-based FSO systems. The chapter introduced the working principle of fibre cables and presented the standard telecommunication fibre cables considered in this study. It then discussed Gaussian beam propagation, emphasising how such beams diverge in the atmosphere. Additionally, the chapter explored the lens parameters used to collimate light from the transmitting fibre and focus it onto the receiving fibre, highlighting their impact on received power. Finally, the chapter addressed the effects of atmospheric turbulence, which include beam wander, loss of spatial coherence, and scintillation.

In Chapter 3, we characterised the transmit performance of the fibre cables by the amount of optical power they transmitted in the Gaussian mode. Transmitting light in the lowest order Gaussian mode proves advantageous due to its reduced divergence, resulting in higher power density at the receiver. Two types of standard SFP transceiver modules (SFP A and B) were used as the light source. This was done to demonstrate that different SFP transceiver modules cannot be naively assumed to be the same.

The power transmitted through the fibre cables when connected to the SFP transceivers

was measured. It was observed that the multi-mode fibre cables transmitted more power from the transceivers compared to the single-mode fibre cables. This can be attributed to their larger dimensions, enabling them to channel more power from the laser in the SFP transceiver. Additionally, it was noted that more power was transmitted through the fibres from SFP B. However, fluctuations in power were more pronounced when the fibre cables were bent, particularly with SFP B, suggesting greater susceptibility to bend losses compared to SFP A.

Subsequently, modal decomposition was employed to determine the modal content of fields launched from the fibre cables. These fields were decomposed into the Orbital Angular Momentum (OAM) basis, with the Gaussian content recorded. A Spatial Light Modulator Spatial Light Modulator (SLM) was utilised in this process to encode holographic filters carrying the conjugate OAM bases. The results of the modal decomposition revealed that, as expected, the single-mode fibre exhibited the highest Gaussian content, while the OM1 fibre had the lowest. Notably, among the multi-mode fibres, the OM5 fibre exhibited the highest Gaussian content. This can be attributed to its greater graded-index profile, which reduces mode coupling and enables it to maintain power in the Gaussian mode. Additionally, the fibre cables displayed higher Gaussian content when connected to SFP A compared to SFP B. The disparity in Gaussian content between the two SFP transceivers, coupled with the observed fluctuations in transmitted power, suggests that light from SFP B comprises more higher-order modes, rendering it more susceptible to mode coupling and bending losses. This underscores the discrepancy in quality between the two transceiver modules. Multiplying the Gaussian content by the total optical power transmitted by the fibre cables provided an approximation of the Gaussian power transmitted by the fibre cables.

In Chapter 4, the focus shifted to the receiver, investigating the impact of misalignment and atmospheric turbulence on coupling into the fibre cables. Three forms of focal point misalignment were considered: lateral, longitudinal, and angular misalignment. The OM1 fibre cable consistently demonstrated superior performance by coupling the highest normalized power across all forms of misalignment. This superiority can be attributed to its larger core size and broader numerical aperture. In contrast, the single-mode fibre cable exhibited the least resilience, coupling the lowest optical power under all considered forms of misalignment. The 50 μm fibre cables displayed similar performance across the different forms of misalignment.

To simulate atmospheric turbulence, phase screens were generated using a sum of weighted Zernike polynomials. These phase screens were encoded onto the SLM. Power coupled into the fibre cables was measured at different turbulence strengths. Results from these measurements revealed that the OM1 fibre cable coupled the highest amount of optical power in the presence of simulated turbulence. The other multi-mode fibre cables exhibited comparable performances, with the OM4 fibre registering the highest average power and the OM3 the lowest among them. The single-mode fibre cable experienced the lowest power coupled under turbulence.

After conducting these measurements, the effects of higher-order aberrations were investigated by excluding tilt aberrations from the generated phase screens, resulting in a reduction in turbulence strength. Under these conditions, all fibre cables demonstrated increased coupling, with the OM1 fibre cable still achieving the highest normalized power. The other multi-mode fibre cables exhibited approximately equal normalized power on average, indicating similar performance in the absence of tilt aberration. Conversely, the single-mode fibre displayed the least tolerance to higher-order aberrations, manifesting the lowest coupled power. The coupling performance under turbulent conditions revealed a relationship between the number of modes a fibre cable can support and its resilience to higher-order aberrations. This was underscored by the similar performance of the standard single-mode fibre and a thermally expanded core single-mode fibre. Despite differences in core size, both single-mode fibres, designed for the Gaussian mode, exhibited similar performance.

Chapter 5 aimed to consolidate these separate characterisations by examining the received power under different transmitting and receiving fibre cable combinations. This was achieved by multiplying the normalized Gaussian power transmitted by the fibre cables, by the normalized average power coupled into them under atmospheric turbulence. In scenarios where equal power is transmitted through all fibre cables, employing a single-mode transmitter and an OM1 receiver yields the most effective performance, while the reverse configuration results in the least favourable outcome. When transmitting from an SFP transceiver, multi-mode fibres transmit more power than the single-mode fibre, leading to increased Gaussian power. Hence, the best performance is achieved when transmitting from an OM5 and receiving into an OM1 fibre cable. This is because the OM5 fibre maintains high Gaussian content while efficiently transmitting high power from the SFP transceiver

In a bidirectional setup, where one type of fibre cable handles both transmission and reception, a consistent pattern emerges in both equal power transmission and transmission from an SFP transceiver. Transmission from an OM1 to an OM1 fibre cable consistently demonstrates superior performance in both scenarios, attributed to its superior coupling ability. The 50 μm core fibre cables yield comparable results, with the OM3 fibre exhibiting the lowest received power among them. Conversely, the single-mode to single-mode configuration results in the worst performance, as this fibre transmits the lowest power from the SFP transceiver and couples the least power under non-ideal conditions.

By assessing the coupling performance of standard fibre cables in free space, this work has demonstrated that such standardised hardware can be utilised for the development of cost-effective FSO systems. Standardised "off-the-shelf" hardware is not only readily available but also significantly reduces both initial costs and maintenance expenses compared to customised electronics designed for high-power lasers. By simplifying system architecture and decreasing manufacturing times, these factors contribute to the overall accessibility and deployability of FSO systems.

The findings of this research will directly impact the design and implementation of SFP-based FSO systems. The results indicate that, in such systems, multi-mode fibre cables should be employed for both transmission and reception, as they transmit and receive higher optical power than single-mode fibre cables. Among the standard telecommunication fibre cables defined in ISO/IEC 11801, this research has shown that transmitting optical signals using an OM5 fibre cable and receiving them through an OM1 fibre cable yields the highest received Gaussian power. For bidirectional applications, transmitting between OM1 fibre cables provides the best results.

While previous SFP-based FSO systems have employed single-mode to multi-mode and single-mode to single-mode transmission configurations [36, 42], this study provides new insights by specifying which fibre cables are used and how they differ in coupling performance. By demonstrating which fibre cable pairings results in the highest received power, this work not only reinforces the feasibility of low-cost implementations but also opens avenues for more efficient designs in future FSO systems.

6.1 Recommendations for future work

This work presents a comparative study of the transmit and coupling performances of standard fibre cables through rigorous experiments. The results presented can inform the design of low-cost SFP transceiver-based FSO systems. To further advance this research, more real-world testing should be conducted. While the OM1, OM4, and OM5 fibres were tested under real-world conditions in the bidirectional setting, the other fibres should also be tested in both unidirectional and bidirectional configurations. The optimal combination of fibres (amongst those tested in this study) for both unidirectional and bidirectional transmission should be tested under real-world conditions across multiple 24-hour testing cycles. Average received power and scintillation indices should be collected to analyse daytime and nighttime performances, considering the fluctuating strength of turbulence.

Furthermore, the system should be tested at different distances to determine its maximum effective range.

A robust outdoor enclosure should be designed to withstand various environmental conditions while remaining cost-effectiveness. It should endure high temperatures and protect against rain, humidity, and dust. Additionally, the enclosure should facilitate easy mounting and installation. Careful consideration should be given to material selection for mounting brackets, flanges, or pole mounts to minimise thermal expansion issues that could lead to misalignment.

The ultimate goal of this work is to contribute to providing high-speed internet connectivity to communities outside the fibre coverage area. Therefore, an SFP-based FSO system should be developed and deployed. Public facilities such as educational institutions and libraries should be prioritised. Ethical data collection from users within these facilities would be useful in assessing the impact and reliability of the deployed FSO system.

References

[1] J. L. Chulilla, "Social and cultural dimensions of digital inclusions," *Int. J. Interact. Multim. Artif. Intell.*, vol. 1, pp. 18–19, 2010.

[2] International Telecommunication Union, *Measuring digital development: Facts and figures 2023*, `https://www.itu.int/hub/publication/d-ind-ict_mdd-2023-1/`, 2023.

[3] L. G. Kazovsky, W. T. Shaw, D. Gutierrez, N. Cheng, and S. W. Wong, "Next-generation optical access networks," *Journal of Lightwave Technology*, vol. 25, pp. 3428–3442, 11 2007.

[4] M. P. Lavery *et al.*, "Tackling africa's digital divide," *Nature Photonics*, vol. 12, no. 5, pp. 249–252, May 2018.

[5] O. Nyarko-Boateng, F. E. B. Xedagbui, A. F. Adekoya, and B. A. Weyori, "Fiber optic deployment challenges and their management in a developing country: A tutorial and case study in ghana," *Engineering Reports*, vol. 2, 2 Feb. 2020.

[6] M. Cox, L. Cheng, and A. Forbes, "Bridging the digital divide: A south african perspective," in *Advanced Photonics 2018*, Optica Publishing Group, 2018, NeW2F.3.

[7] T. PALANIVEL, *Rapid urbanisation: Opportunities and challenges to improve the well-being of societies*, https://hdr.undp.org/content/rapid-urbanisation-opportunities-and-challenges-improve-well-being-societies, Sep. 2017.

[8] A. Trichili, M. Cox, B. Ooi, and M.-S. Alouini, "Roadmap to free space optics," *Journal of the Optical Society of America B*, vol. 37, Jul. 2020.

[9] A. Sabri, S. Hameed, and W. Hadi, "Last mile access-based fso and vlc systems," *Applied Optics*, vol. 62, Oct. 2023.

[10] G. Hörack, P. Pezzei, E. Leitgeb, and M. Tischlinger, "Economic aspects of free space optics as an alternative broadband network connection for the last mile," in *2016 10th International Symposium on Communication Systems, Networks and Digital Signal Processing (CSNDSP)*, 2016.

[11] A. G. Alkholidi and K. S. Altowij, "Free space optical communications — theory and practices," in *Contemporary numbers in Wireless Communications*, Rijeka: IntechOpen, Jan. 2014, ch. 5.

[12] H. Kaushal, V. Jain, and S. Kar, *Optical Networks: Free Space Optical Communication*, B. Mukherjee, Ed. Springer, 2017.

[13] J. Hecht, "The first half-century of laser development," *Laser Technik Journal*, vol. 7, pp. 20–25, 4 Jul. 2010.

[14] F. E. Goodwin, "A review of operational laser communication systems," *Proceedings of the IEEE*, vol. 58, no. 10, pp. 1746–1752, 1970.

[15] A. Lorences-Riesgo, F. P. Guiomar, A. N. Sousa, A. L. Teixeira, N. J. Muga, and P. P. Monteiro, "200 gbit/s free-space optics transmission using a kramers-kronig receiver," *Optical Fiber Communication Conference (OFC) 2019*, 2019.

[16] R. Lange, B. Smutny, B. Wandernoth, R. Czichy, and D. Giggenbach, "142 km, 5.625 gbps free-space optical link based on homodyne bpsk modulation," in *Free-Space Laser Communication Technologies XVIII*, vol. 6105, SPIE, Feb. 2006.

[17] N. Cvijetic, D. Qian, J. Yu, Y. K. Huang, and T. Wang, "Polarization-multiplexed optical wireless transmission with coherent detection," *Journal of Lightwave Technology*, vol. 28, no. 8, pp. 1218–1227, 2010.

[18] H. W. Wu, C. Y. Li, H. H. Lu, Q. P. Huang, S. C. Tu, and Y. C. Huang, "A pdm-based 128-gb/s pam4 fibre-fso convergent system with obpfs for polarisation de-multiplexing," *Scientific Reports*, vol. 10, no. 1, Dec. 2020.

[19] H.-H. Lu *et al.*, "800 gb/s/200 m fso link with a wdm-pam4 scheme and slm-based beam tracking technology," *Optics Letters*, vol. 46, no. 6, p. 1269, Mar. 2021.

[20] H. H. Lu *et al.*, "A two-way 224-gbit/s pam4-based fibre-fso converged system," *Scientific Reports*, vol. 12, no. 1, Dec. 2022.

[21] H.-H. Lu, C.-Y. Li, M.-T. C. Chun-Ming Ho, X.-Y. Lin, Z.-Y. Yang, and H.-W. Chen, "64 gb/s pam4 vcsel-based fso link," *Optics Express*, vol. 25, no. 5, p. 5749, Mar. 2017.

[22] C.-Y. Li *et al.*, "A flexible bidirectional fiber-fso-5g wireless convergent system," *Journal of Lightwave Technology*, vol. 39, no. 5, 2021.

[23] M. A. Khalighi and M. Uysal, "Survey on free space optical communication: A communication theory perspective," *IEEE Communications Surveys and Tutorials*, vol. 16, pp. 2231–2258, 4 Apr. 2014.

[24] X. Nghatsane, L. Cheng, and M. Cox, "Fritchman modeling for correlated turbulence-induced errors in fso communication," *Applied Optics*, vol. 60, Mar. 2021.

[25] S. Abe *et al.*, "Short wave sff small form factor transceivers," in *2001 Proceedings. 51st Electronic Components and Technology Conference (Cat. No.01CH37220)*, 2001, pp. 30–34.

[26] W. Hogan, D. Gaio, M. Cohen, and J. Trewhella, "A novel low-cost small-form-factor transceiver module," Feb. 2000, pp. 725–732.

[27] H. J. Yoon and J. G. Kim, "622-mb/s bidirectional sfp optical transceiver using an integrated wdm optical subassembly," *IEEE Transactions on Advanced Packaging*, vol. 31, pp. 423–428, 2 May 2008.

[28] SFF Committee, "Small form-factor pluggable (sfp) transceiver multisource agreement (msa)," SNIA, Santa Clara CA, Standard INF-8074, May 2001.

[29] D. Zheng *et al.*, "Free-space to few-mode-fiber coupling under atmospheric turbulence," *Optics Express*, vol. 24, pp. 18 739–18 744, Aug. 2016.

[30] Y. Dikmelik and F. M. Davidson, "Fiber-coupling efficiency for free-space optical communication through atmospheric turbulence," *Applied Optics*, vol. 44, no. 23, pp. 4946–4952, Aug. 2005.

[31] Q. Yang *et al.*, "Effects of atmospheric turbulence on fiber-coupled dpsk system in satellite-to-ground downlink," *Results in Physics*, vol. 11, pp. 938–943, Dec. 2018.

[32] M. Toyoshima, "Maximum fiber coupling efficiency and optimum beam size in the presence of random angular jitter for free-space laser systems and their applications," *Journal of the Optical Society of America. A, Optics, image science, and vision*, vol. 23, pp. 2246–50, Oct. 2006.

[33] L. Tan *et al.*, "Optimal coupling condition analysis of free-space optical communication receiver based on few-mode fiber," *Optical Fiber Technology*, vol. 53, p. 102 004, Dec. 2019.

[34] X. Long, B. Qi, G. Ren, S. Wang, H. Ma, and J. Bian, "Simulation study on fiber-coupling efficiency for quantum communication through atmospheric turbulence," in *XX International Symposium on High-Power Laser Systems and Applications 2014*, vol. 9255, SPIE, Feb. 2015.

[35] M. Zhu, Y. Shen, A. Chiluisa, J. Song, L. Fichera, and Y. Liu, "Optical fiber coupling system for steerable endoscopic instruments," in *Annu Int Conf IEEE Eng Med Biol Soc.*, Nov. 2021, pp. 4871–4874.

[36] L. Mustafa and B. Thomsen, "Reintroducing free-space optical technology to community wireless networks," in *19th Americas Conference on Information Systems, AMCIS 2013, Chicago, Illinois, USA, August 15-17, 2013*, Association for Information Systems, 2013.

[37] M. M. Abadi, Z. Ghassemlooy, N. Mohan, S. Zvanovec, M. R. Bhatnagar, and R. Hudson, "Implementation and evaluation of a gigabit ethernet fso link for 'the last metre and last mile access network'," in *2019 IEEE International Conference on Communications Workshops (ICC Workshops)*, Shanghai: Institute of Electrical and Electronics Engineers, May 2019.

[38] M. Curran *et al.*, "Fsonet: A wireless backhaul for multi-gigabit picocells using steerable free space optics," in *Proceedings of the Annual International Conference on Mobile Computing and Networking*, Association for Computing Machinery, May 2017, pp. 154–166.

[39] M. M. Abadi, M. A. Cox, R. E. Alsaigh, S. Viola, A. Forbes, and M. P. Lavery, "A space division multiplexed free-space-optical communication system that can auto-locate and fully self align with a remote transceiver," *Scientific Reports*, vol. 9, no. 1, Dec. 2019.

[40] J. N. Kutz, J. A. Cox, and D. Smith, "Mode mixing and power diffusion in multimode optical fibers," *Journal of Lightwave Technology*, vol. 16, 7 1998.

[41] H. J. Eichler, B. Liu, M. Duelk, Z. Lu, and J. Chen, "Phase conjugation behind an ordered multimode fibre bundle," *Optics Communications*, vol. 123, p. 412 422, Jan. 1996.

[42] J. P. Agrawal, O. Farook, and C. R. Sekhar, "Designing a free-space optical/wireless link," in *American Society for Engineering Education Annual Conference and Exposition*, American Society for Engineering Education, 2004.

[43] ISO Central Secretariat, "Information technology — generic cabling for customer premises," en, International Organization for Standardization, Geneva, CH, Standard ISO/IEC 11801-1:2017, Nov. 2017.

[44] A. Jurado-Navas, A. Tatarczak, X. Lu, J. J. V. Olmos, J. M. Garrido-Balsells, and I. T. Monroy, "850-nm hybrid fiber/free-space optical communications using orbital angular momentum modes," *Optics Express*, vol. 23, no. 26, pp. 33 721–33 732, Dec. 2015.

[45] C. A. Bunge, M. Beckers, and B. Lustermann, "Basic principles of optical fibres," in *Polymer Optical Fibres: Fibre Types, Materials, Fabrication, Characterisation and Applications*. Elsevier Inc., 2017, pp. 47–118.

[46] W. Shieh and I. Djordjevic, "Optical communication fundamentals," in *OFDM for Optical Communications*, Elsevier, 2010, pp. 53–118.

[47] J. Alda, "Laser and gaussian beam propagation and transformation," *Encyclopedia of Optical Engineering*, Jan. 2003.

[48] P. Joachim, "Optical waves," in Elsevier, 2003, pp. 83–120.

[49] A. Siegman, *Lasers* (University Science Bks). University Science Books, 1986.

[50] T. S. Khwaja and S. A. Reza, *Power transmittance of a laterally shifted gaussian beam through a circular aperture*, 2016. arXiv: 1605.04241 [physics.gen-ph].

[51] H. Kaushal and G. Kaddoum, "Free space optical communication: Challenges and mitigation techniques," *CoRR*, vol. abs/1506.04836, Jun. 2015. arXiv: 1506.04836.

[52] A. Hamza, J. Deogun, and D. Alexander, "Classification framework for free space optical communication links and systems," *IEEE Communications Surveys and Tutorials*, Oct. 2018.

[53] S. Al-Gailani *et al.*, "A survey of free space optics (fso) communication systems, links, and networks," *IEEE Access*, Dec. 2020.

[54] Z. Ghassemlooy and W. O. Popoola, "Terrestrial free-space optical communications," in *Mobile and Wireless Communications network Layer and Circuit Level Design*, London, United Kingdom: IntechOpen, Jan. 2010, ch. 17, pp. 355–392.

[55] M. A. Cox, L. Gailele, L. Cheng, and A. Forbes, "Modelling the memory of turbulence-induced beam wander," Jul. 2019.

[56] L. C. Andrews, R. L. Phillips, and S. of Photo-optical Instrumentation Engineers., *Laser beam propagation through random media*, 2nd ed. SPIE, 2005, p. 782.

[57] V. P. Aksenov, V. V. Dudorov, V. V. Kolosov, and V. Y. Venediktov, "Probability distribution of intensity fluctuations of arbitrary-type laser beams in the turbulent atmosphere," *Optics Express*, vol. 27, no. 17, pp. 24 705–24 716, Aug. 2019.

[58] D. Chen and J. Hui, "Parameter estimation of gamma–gamma fading channel in free space optical communication," *Optics Communications*, vol. 488, p. 126 830, 2021.

[59] R. Scheps, *Introduction to Laser Diode-Pumped Solid State Lasers*, 1st ed. SPIE Publications, Jan. 2002, vol. TT53.

[60] D. Marcuse, "Loss analysis of single-mode fiber splices," *The Bell system technical journal*, vol. 56, pp. 703–718, 5 Jun. 1977.

[61] A. Argyros, R. Lwin, and M. C. Large, "Bend loss in highly multimode fibres," *Optics Express*, vol. 16, no. 23, pp. 18 590–18 598, Nov. 2008.

[62] L. Jeunhomme and J. P. Pocholle, "Mode coupling in a multimode optical fiber with microbends," *Applied Optics*, vol. 14, no. 10, pp. 2400–2405, Oct. 1975.

[63] S. Savović, A. Djordjevich, A. Simovic, and B. Drljača, "Influence of mode coupling on three spatially multiplexed channels in multimode graded index plastic optical fibers," *Laser Physics*, vol. 30, 115102 (5pp), Oct. 2020.

[64] G. Stepniak, L. Maksymiuk, and J. Siuzdak, "Influence of mode coupling on mode group diversity multiplexing in multimode fibers," *Optical and Quantum Electronics*, vol. 41, pp. 203–213, 3 Feb. 2009.

[65] J. P. Koplow, D. A. V. Kliner, and L. Goldberg, "Single-mode operation of a coiled multimode fiber amplifier," *Optics Letters*, vol. 25, no. 7, pp. 442–444, Apr. 2000.

[66] J. Pinnell, I. Nape, B. Sephton, M. A. Cox, V. Rodríguez-Fajardo, and A. Forbes, "Modal analysis of structured light with spatial light modulators: A practical tutorial," *Journal of the Optical Society of America A*, vol. 37, no. 11, pp. C146–C160, Nov. 2020.

[67] C. Schulze, A. Dudley, D. Flamm, M. Duparré, and A. Forbes, "Measurement of the orbital angular momentum density of light by modal decomposition," *New Journal of Physics*, vol. 15, no. 7, p. 073 025, Jul. 2013.

[68] T. Kaiser, D. Flamm, S. Schröter, and M. Duparré, "Complete modal decomposition for optical fibers using cgh-based correlation filters," *Optics Express*, vol. 17, no. 11, pp. 9347–9356, May 2009.

[69] J. Pinnell, V. Rodríguez-Fajardo, and A. Forbes, "Single-step shaping of the orbital angular momentum spectrum of light," *Optics Express*, vol. 27, p. 28 009, 20 Sep. 2019.

[70] M. Oral and U. Deniz, "Centre of mass model - a novel approach to background modelling for segmentation of moving objects," *Image and Vision Computing*, vol. 25, pp. 1365–1376, 8 Aug. 2007.

[71] O. Shapira, A. F. Abouraddy, J. D. Joannopoulos, and Y. Fink, "Complete modal decomposition for optical waveguides," *Physical Review Letters*, vol. 94, 14 Apr. 2005.

[72] D. Kedar and S. Arnon, "Urban optical wireless communication networks: The main challenges and possible solutions," *IEEE Communications Magazine*, vol. 42, 5 May 2004.

[73] J. Ma, F. Zhao, L. Tan, S. Yu, and Y. Yang, "Degradation of single-mode fiber coupling efficiency due to localized wavefront aberrations in free-space laser communications," *Optical Engineering - OPT ENG*, vol. 49, no. 4, p. 045 004, Apr. 2010.

[74] L. Ma, S. Gao, B. Chen, and Y. Liu, "Theoretical and experimental analysis on statistical properties of coupling efficiency for single-mode fiber in free-space optical communication link based on non-kolmogorov turbulence," *Applied Sciences (Switzerland)*, vol. 12, no. 12, p. 6075, Jun. 2022.

[75] P. J. Winzer and W. R. Leeb, "Fiber coupling efficiency for random light and its applications to lidar," *Optics Letters*, vol. 23, no. 13, 1998.

[76] Y. Bian *et al.*, "Free-space to single-mode fiber coupling efficiency with optical system aberration and fiber positioning error under atmospheric turbulence," *Journal of Optics (United Kingdom)*, vol. 24, no. 2, Feb. 2022.

[77] A. H. Al-Hamdani, H. G. Rahid, Z. Rashed, H. G. Rashid, and Z. R. Ghayib, "Improvement of laser to fiber coupling efficiency using microlens technique," *ARPN Journal of Engineering and Applied Sciences*, vol. 9, 11 Nov. 2014.

[78] J. Schmidt, *Numerical simulation of optical wave propagation: With examples in MATLAB*. SPIE Press, Jan. 2010.

[79] R. J. Noll, "Zernike polynomials and atmospheric turbulence," *Journal of the Optical Society of America*, vol. 66, no. 3, p. 207, Mar. 1976.

[80] V. Lakshminarayanan and A. Fleck, "Zernike polynomials: A guide," *Journal of Modern Optics*, vol. 58, pp. 1678–1678, Apr. 2011.

[81] L. Burger, I. A. Litvin, and A. Forbes, "Simulating atmospheric turbulence using a phase-only spatial light modulator," *South African Journal of Science*, vol. 104, pp. 129–134, 2008.

[82] M. A. Cox, C. Rosales-Guzmán, M. P. J. Lavery, D. J. Versfeld, and A. Forbes, "On the resilience of scalar and vector vortex modes in turbulence," *Optics Express*, vol. 24, no. 16, p. 18 105, Jul. 2016.

[83] Z. Zhao *et al.*, "Modal coupling and crosstalk due to turbulence and divergence on free space thz links using multiple orbital angular momentum beams," *Scientific Reports*, vol. 11, 1 Dec. 2021.

[84] R. Racine, "The strehl efficiency of adaptive optics systems," *Publications of the Astronomical Society of the Pacific*, vol. 118, pp. 1066–1075, Jul. 2006.

[85] M. P. J. Lavery *et al.*, "Free-space propagation of high-dimensional structured optical fields in an urban environment," *Science Advances*, vol. 3, e1700552, 10 Oct. 2017.